

Photodissociation dynamics of formaldehyde: H₂ rotational distributions and product quantum state correlations

Thomas J. Butenhoff, Karen L. Carleton, and C. Bradley Moore

Citation: *The Journal of Chemical Physics* **92**, 377 (1990); doi: 10.1063/1.458440

View online: <http://dx.doi.org/10.1063/1.458440>

View Table of Contents: <http://scitation.aip.org/content/aip/journal/jcp/92/1?ver=pdfcov>

Published by the [AIP Publishing](#)

Articles you may be interested in

[Photodissociation dynamics of acetylacetone: The OH product state distribution](#)

J. Chem. Phys. **110**, 11850 (1999); 10.1063/1.479126

[The correlated product state distribution of ketene photodissociation at 308 nm](#)

J. Chem. Phys. **104**, 7460 (1996); 10.1063/1.471459

[Photodissociation dynamics of formaldehyde: H₂ \(v,J\) vector correlations](#)

J. Chem. Phys. **93**, 3907 (1990); 10.1063/1.458777

[Dynamics of H₂O₂ photodissociation: OH product state and momentum distribution characterized by sub-Doppler and polarization spectroscopy](#)

J. Chem. Phys. **85**, 4463 (1986); 10.1063/1.451767

[Rotational state distributions of H₂ and CO following the photofragmentation of formaldehyde](#)

J. Chem. Phys. **84**, 1487 (1986); 10.1063/1.450494



Photodissociation dynamics of formaldehyde: H₂ rotational distributions and product quantum state correlations

Thomas J. Butenhoff, Karen L. Carleton, and C. Bradley Moore
Department of Chemistry, University of California, Berkeley, California 94720

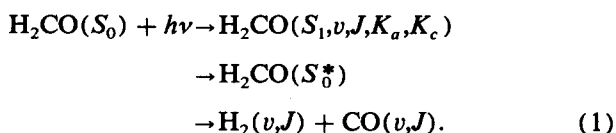
(Received 9 August 1989; accepted 20 September 1989)

The alignment and rotational state populations of *ortho* and *para* H₂ ($v = 1$) and H₂ ($v = 3$) produced from formaldehyde photolysis near the threshold for dissociation are measured with Doppler-resolved laser-induced fluorescence spectroscopy in the vacuum ultraviolet (VUV). A single rovibronic level of the first excited singlet state of H₂CO in a molecular jet is excited by a pulsed UV laser and the H₂ is probed under collisionless conditions with VUV generated by third harmonic generation in Kr or Xe. The rotation of the excited H₂CO during the 10⁻⁷–10⁻⁸ s before dissociation does not completely wash out the alignment: e.g., photolysis on the 2¹4¹ ¹R₀(0)*e* H₂CO line produces H₂ ($v = 3, J = 2$) with $A_0^{(2)} = -0.31 \pm 0.06$. The *ortho* and *para* H₂ rotational distributions lie on a single smooth curve peaked at $J \approx 3$. The H₂CO(*S*₁) vibrational state has little influence on the J_{H_2} distributions, but there is evidence that photolysis of higher rotational states of H₂CO(*S*₁) results in warmer J_{H_2} distributions. The Doppler profiles enable the measurement of the H₂ (v, J) average velocities. Conservation of energy and linear momentum permit the corresponding CO J state to be calculated. H₂ formed in high vibrational states is correlated with CO formed in low rotational states. A three-parameter, semiclassical model which combines an impulsive force with the momenta of zero-point vibrations of the parent near or at the transition state geometry reproduces all of the general features of the H₂ (v, J) and CO (v, J) distributions from H₂CO photolysis near the barrier to dissociation.

I. INTRODUCTION

Formaldehyde is one of a few small molecular systems which has been intensively studied both experimentally and theoretically. The reaction dynamics can be unraveled in great detail as all photodissociation products can be probed.¹⁻⁵ This system is also theoretically tractable with state-of-the-art *ab initio* techniques.⁶⁻⁹

This combination of experiment and theory has already yielded a wealth of information on product distributions. The mechanism for molecular dissociation is well known¹:



The electronically excited H₂CO internally converts to highly excited vibrational levels of the ground electronic state, where it dissociates over a steep barrier. This process has been studied by measuring the CO vibrational distribution,² the CO (v, J) distribution by laser-induced fluorescence (LIF),³ the *ortho* H₂ (v, J) distribution by coherent anti-Stokes Raman spectroscopy (CARS),^{4,5} and the translational energy distribution by time-of-flight mass spectrometry.¹⁰ For photolysis energies near the barrier to dissociation, the CO product is highly rotationally excited with little vibrational energy (88% in $v = 0$).² The H₂ vibrational distribution peaks at $v = 1$ and the rotational distribution is approximately Boltzmann-like with T_{rot} decreasing as the vibrational state increases. Most of the available energy released (65%) appears as H₂ translational energy. The

CO (v, J) and H₂ (v, J) populations together with the measured translational energy distribution suggest that there may be a correlation between CO rotational states and H₂ vibrational states.⁴ This correlation may arise from angular momentum conservation together with an impact parameter constraint in the fragmenting H₂CO transition state.

The previous H₂ and CO experiments were carried out in room temperature flow cells where more than one H₂CO(*S*₁) rotational state was excited. In the CARS experiments,^{4,5} H₂ products were translationally cooled with helium buffer gas prior to detection in order to improve the signal-to-noise ratio. The H₂ rotational population results were corrected approximately for translational-to-rotational energy transfer caused by high velocity H₂-He collisions. All translational energy information was lost in this experiment.

The CO studies examined the effect of the H₂CO(*S*₁) rotational energy on the final CO (v, J) distribution. For an increase in H₂CO(*S*₁) J state from 3 to 15, the peak in the CO rotational distribution remained the same, $J = 42$, and the FWHM of the J distribution broadened only slightly.

Several theoretical studies have examined the photodissociation of formaldehyde. *Ab initio* calculations found the transition state geometry to be bent and planar, and the reaction coordinate suggests a large impact parameter.^{6,7} This is consistent with the large amount of CO rotational excitation observed experimentally. The product state distributions have been calculated using an elegant theory by Schinke.¹¹⁻¹³ The calculations model the effects of the initial H₂CO(*S*₀^{*}) state by using the in-plane vibrational displacement amplitudes of the transition state geometry as well as an *ab initio*

$\text{H}_2\text{-CO}$ exit valley potential energy surface.^{11,12} By applying the infinite order sudden approximation, Schinke reproduces the highly peaked CO rotational distributions measured for all three isotopic species (H_2CO , HDCO, and D_2CO)¹² and matches the CARS *ortho* H_2 rotational distribution reasonably well.¹¹ He further predicts the distributions for *para* H_2 to be bimodal, peaking at both $J = 0$ and 9.

The present experiments measure H_2 rotational distributions and alignment in a molecular jet under collisionless conditions using Doppler-resolved laser-induced fluorescence spectroscopy. H_2 LIF detection has excellent sensitivity and allows the measurement of both the *ortho* and *para* H_2 J distributions for comparison with Schinke's theoretical predictions.¹¹ The Doppler-resolved profiles provide average translational energies for each H_2 rovibrational state, which provide product quantum state correlations.¹⁴ The effect of the initial rotational and vibrational states of the excited $\text{H}_2\text{CO}(S_1)$ is also studied.

II. EXPERIMENTAL

The experiments were carried out in a diffusion-pumped, cryogenically trapped chamber with a pulsed free jet (Fig. 1). The photolysis and probe lasers operated at 10 Hz and were counterpropagating and orthogonal to the free jet and fluorescence detection axes. The vacuum ultraviolet (VUV) light was generated by third harmonic generation (THG) in a cell of krypton or xenon and the VUV as well as the residual UV entered the chamber through a LiF window. The conversion efficiency of THG in rare gases is $\approx 10^{-6}$.¹⁵ Photomultipliers (PMT) detect H_2CO fluorescence and VUV power for H_2 signal normalization.

A. Sample

H_2CO monomer was produced in the usual way.¹⁶ A mixture of 9 Torr H_2CO seeded in 300 Torr He was prepared

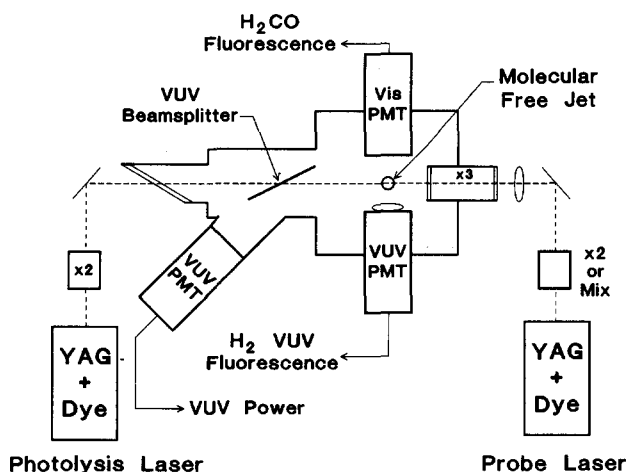


FIG. 1. Experimental apparatus showing counterpropagating photolysis and probe lasers, Kr or Xe cell for VUV generation ($\times 3$), H_2CO free jet pointed into the page, and PMTs for detection of H_2 VUV fluorescence, H_2CO fluorescence, and VUV power. The photolysis laser entrance window is at Brewster's angle and is rotated to be P polarized with respect to the photolysis laser polarization. The VUV beamsplitter and VUV normalization PMT are rotated to keep the beamsplitter S polarized with respect to the VUV polarization.

by flowing He over the liquid monomer contained in a U-tube immersed in a -89°C slush of n -butanol cooled by liquid nitrogen. This mixture was expanded through the 0.8 mm aperture of the pulsed valve (General Valve) to produce 0.5–2 ms pulses at a 10 Hz repetition rate. The background pressure in the chamber was 2×10^{-5} Torr when the nozzle was running under typical experimental conditions. Analysis of the H_2CO fluorescence excitation spectrum, taken with low laser power (0.4 mJ/pulse) to minimize saturation, yielded a formaldehyde rotational temperature of 4–6 K.

B. H_2CO photolysis

The photolysis laser was a Nd:YAG pumped dye laser (Quantel TDL-50, DCM/LDS-698 dye mixture, 10 Hz) frequency doubled in a static KDP crystal to produce 4–5 mJ per ≈ 7 ns pulse. The UV bandwidth was 0.2 cm^{-1} (FWHM) as determined from the H_2CO fluorescence excitation spectra. The laser beam had a 4 mm diameter in the interaction region. H_2CO fluorescence was detected by a photomultiplier tube (9813QB EMI) mounted on the axis mutually orthogonal to both the molecular beam and the laser beam axes. Filters ($370 < \lambda_{\text{pass}} < 490\text{ nm}$) and a series of apertures were used to reduce scattered light. The signal was sent to a gated integrator and a computer for normalizing the H_2 product signals directly by the number density of excited H_2CO , thus compensating for photolysis laser frequency and intensity fluctuations. After summing over 5 scans, H_2CO fluorescence intensity fluctuations were between 5% and 15%, and the average fluorescence signal varied by less than 20% on any particular day.

Formaldehyde was excited to several rovibrational levels of the S_1 manifold. The 4^1 , 4^3 , and $2^1 4^1$ vibrational bands were studied,¹⁷ where ν_4 is the out-of-plane bend and ν_2 is the CO stretch. Because of conservation of nuclear spin during dissociation,^{4,18} *para* and *ortho* H_2 (even and odd J) are produced by photolysis of *para* and *ortho* H_2CO (even and odd K_a), respectively. Therefore, the complete product distribution can only be measured by photolysis on two separate H_2CO transitions. *Para* formaldehyde was typically excited on the ${}^rR_0(0)e$ line ($1_{11} \leftarrow 0_{00}$).¹⁹ *Ortho* formaldehyde was excited on several $J_{K_a K_c}$ lines, including the unresolved ${}^rR_1(1)e + o(2_{20}, 2_{21} \leftarrow 1_{10})$ lines and the ${}^p p_1(1)o(0_{00} \leftarrow 1_{11})$ line. All H_2CO lines were assigned using the spectroscopic constants given in Ref. 20.

C. H_2 LIF excitation spectroscopy

The dissociation products were probed 50–100 ns after photolysis. Different VUV wavelength regions were needed to probe the different H_2 vibrational states. In all cases, a Nd:YAG pumped dye laser (Quantel model 531C and TDL-50) provided tunable visible light. The visible light was doubled or mixed with the YAG fundamental to generate ≈ 7 ns pulse length UV light. The UV was focused by a 15 cm lens into a 2.5 cm diameter, 10.5 cm long stainless steel cell containing either Kr or Xe to generate VUV via third harmonic generation (THG). The optimum rare gas pressure is a function of wavelength and was varied to maximize VUV output. The VUV and residual UV exited the cell directly

into the chamber through a 2 mm thick LiF window and was overlapped with the photolysis laser. The probe beam size was approximately 3 mm diameter in the interaction region as estimated from the UV beam fluorescence from a white card. The UV produced no resonant background signals.

All of the H_2 transitions were assigned using Ref. 21. H_2 ($v = 0$) was probed on the (3,0), (4,0), and (5,0) bands of the $B^1\Sigma_u^+ \leftarrow X^1\Sigma_g^+$ transition. The dye laser output (DCM) was frequency doubled in an autotracking KD*P crystal (Inrad) to produce 6–8 mJ UV which was focussed into the cell filled with 3–40 Torr Xe to generate light from 106.2–106.7 nm.^{15,22} The UV was not separated from the residual visible light because suitable dichroic mirrors were not available and our best cutoff filters transmitted only 80% of the UV light (THG efficiency is proportional to the UV power cubed). H_2 lineshapes were compared with and without the residual visible light and there were no differences.

H_2 ($v = 1$) was probed on the (4,1), (3,1), and (2,1) bands of the $B^1\Sigma_u^+ \leftarrow X^1\Sigma_g^+$ transition, and H_2 ($v = 2$) was probed on the $B^1\Sigma_u^+ \leftarrow X^1\Sigma_g^+$ (6,2) band and on the $C^1\Pi_u^+ \leftarrow X^1\Sigma_g^+$ (0,2) band. The dye laser output (LDS-698/DCM mixture) was frequency doubled to produce 5–8 mJ of UV which was separated from the residual visible light with dichroic mirrors. The UV was focused into the cell containing 70–260 Torr Kr to generate light from 110–116 nm.^{23,24}

H_2 ($v = 3$) was probed on the (0,3) and (1,3) bands of the $B^1\Sigma_u^+ \leftarrow X^1\Sigma_g^+$ transition. The dye laser output (R640/R610 mixture) was frequency-sum mixed with the Nd:YAG fundamental in an autotracking KD*P crystal (Quanta Ray WEX). The resulting 7–10 mJ of UV was spatially separated from the Nd:YAG fundamental and the dye laser output with a Pellin–Broca prism. The UV was focused into the cell filled with 5–100 Torr Xe to generate VUV from 127–129 nm. The Pellin–Broca prism was adjusted at the different wavelengths to maintain the probe beam alignment through the chamber.

H_2 VUV fluorescence was detected with a solar blind photomultiplier tube (EMR 542G, MgF₂ window) mounted in the vacuum at right angles to the laser and molecular beams (opposite the H_2 CO fluorescence PMT). The 2.9 cm diameter cathode of the PMT was 5 cm from the jet axis. The $B^1\Sigma_u^+ \rightarrow X^1\Sigma_g^+$ fluorescence occurs at wavelengths greater than 135 nm and was collected with a 2.2 cm diameter $f/1$ CaF₂ lens mounted 2.2 cm from the molecular jet. This increased signal collection and also discriminated against scattered VUV light. The $C^1\Pi_u^+ \rightarrow X^1\Sigma_g^+$ fluorescence occurs at wavelengths similar to the excitation wavelengths and was collected through a 2 mm thick VUV-grade MgF₂ window/filter. The signal was amplified (Pacific 2A50), averaged with a boxcar (Stanford Research SR250), and sent to the computer.

The VUV power was measured by reflecting a fraction of the probe beam with a LiF flat onto a solar blind photomultiplier tube (EMR 542G, LiF window). The VUV light had a 70° angle of incidence and was *S* polarized with respect to the flat. To avoid PMT saturation, 6–8 layers of fine Nickel wire mesh were placed in front of the normalization PMT

to act as a line of sight filter. This PMT has an unusually low quantum yield for UV and was insensitive to the UV light which was also incident on the PMT. After summing 5 scans, VUV intensity fluctuations were between 15% and 40% for a given scan and the average power varied by as much as a factor of 5 over the VUV generation tuning range.

The VUV fluorescence, VUV normalization, and H_2 CO fluorescence signals were integrated by boxcar, typically averaging three shots, and sent to the computer. Each H_2 rovibrational line was scanned five times and these scans were then added. The resulting VUV fluorescence signal was normalized for VUV power and H_2 CO fluorescence at each of 600–800 points across the 0.025 nm (VUV) scan. The same computer triggered the pulsed nozzle, triggered the Nd:YAG lasers, and scanned the dye laser.

The laser beams intersected the jet axis 1.6 cm from the nozzle. The probe distance from the nozzle was adjusted to ensure that the H_2 products were probed under collisionless conditions. This was assured by working in the region where the H_2 Doppler profiles were independent of the distance of the probe laser from the nozzle. When the probe distance from the nozzle was increased to 2.0 cm, the measured line shape parameters were within the 5% uncertainty of a single measurement. Noticeable differences in the lineshapes occurred for probe distances less than 1.3 cm from the nozzle.

The polarizations of the photolysis and probe lasers were varied by changing the configuration of the steering mirrors or prisms. Both laser polarizations were measured at the chamber with a Glan–Thompson polarizer and were found to be linear.

H_2 CO has sharp absorption and VUV LIF emission features in the range of 112.9–115.1 nm which overlap a few of the Doppler broadened H_2 ($v = 1$) lines. The sharpest of these H_2 CO lines was fit to a Gaussian and the FWHM was considered to be equal to the convolution of the VUV bandwidth and parent velocity distribution FWHM. The VUV bandwidth/parent velocity convolution near 106.7 nm was determined by measuring LIF excitation spectra of jet cooled H_2 seeded in He. The rising and falling edges of square and dipped Doppler broadened H_2 LIF peaks are fit well with these measured VUV bandwidths. The VUV bandwidth in the range of 127–129 nm was estimated from the edges of square and dipped H_2 ($v = 3$) Doppler broadened LIF lines. In the course of these experiments, the VUV FWHM bandwidth varied from 1.0–1.5 cm^{-1} .

III. ANALYSIS AND RESULTS

H_2 LIF Doppler profiles are measured for three different excitation-detection geometries (Fig. 2). The H_2 LIF data is analyzed to obtain both population distributions and vector correlations for formaldehyde photodissociation. To obtain both peak intensities and line shape parameters, the normalized H_2 signals are fit to the line shape profile given by Dixon^{25,26}:

$$g(\chi) = \frac{I}{2\Delta v_D} [1 + \beta_{er} P_2(\cos \theta) P_2(\chi)], \quad (2)$$

where the narrow product velocity distribution is approximated as a single velocity. Here, I is the integrated peak

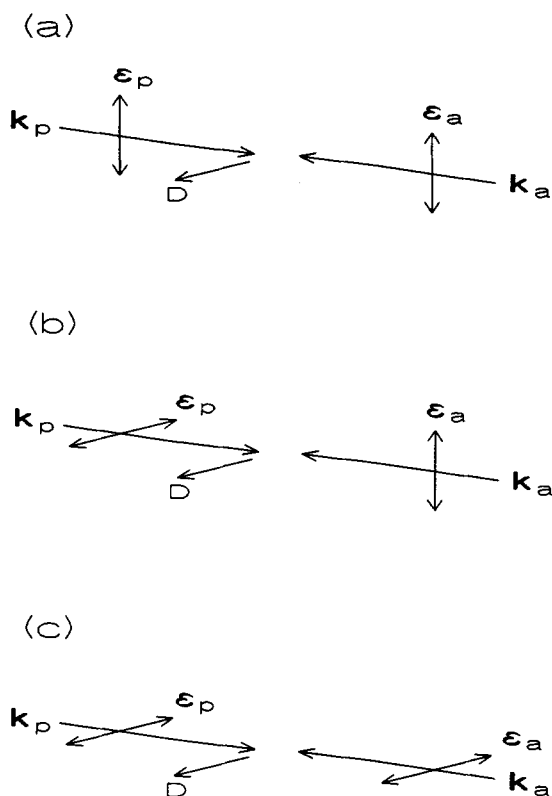


FIG. 2. The photolysis (k_p , ϵ_p) and probe (k_a , ϵ_a) laser beam geometries: k and ϵ are the laser propagation directions and polarizations; the detector D detects all polarizations. Case (a) is a mutually orthogonal geometry; case (b) is the coaxially detected geometry with ϵ_a perpendicular to ϵ_p ; case (c) is the coaxially detected geometry with ϵ_a parallel to ϵ_p .

intensity, $\Delta\nu_D = \nu_0 v/c$ is the maximum Doppler shift (ν_0 is the line center and v is the average product velocity), β_{eff} is the effective lineshape parameter, $P_2(x) = (3x^2 - 1)/2$ is the second Legendre polynomial, θ is the angle between the photolysis polarization and the probe laser propagation axis, and χ is the ratio of the Doppler shift to the maximum Doppler shift [$\chi = (\nu - \nu_0)/\Delta\nu_D$]. The resulting fit parameters are the maximum Doppler shift $\Delta\nu_D$ which gives the average velocity for a given H_2 rovibrational state, the line shape parameter β_{eff} which gives the vector correlations,^{25,27,28} and the integrated intensity I . The fits include convolution with the Gaussian determined in Sec. II C to account for the probe laser bandwidth and the initial parent velocities. Sample data for H_2 ($J = 1$) along with the line shape fits are shown in Fig. 3.

A. Product populations and alignments

The H_2 rotational populations for a given H_2 vibrational state and product $\text{H}_2(v, J)$ alignments are determined from the LIF peak intensities using the expression^{29,30}

$$I = C_{\text{H}_2}(J'')S\nu G [b_0 + (5/4)b_1 A_0^{(2)}], \quad (3)$$

where I is the integrated LIF peak intensity normalized for VUV power and $\text{H}_2\text{CO}(S_1)$ number density, $C_{\text{H}_2}(J'')$ is proportional to the $\text{H}_2(J'')$ population, $A_0^{(2)}$ is the align-

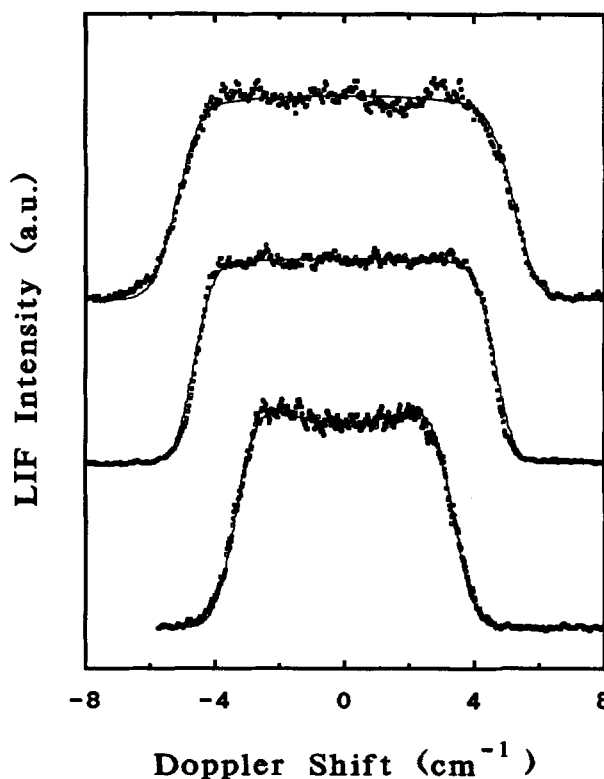


FIG. 3. $B^1\Sigma_u^+ \leftarrow X^1\Sigma_g^+$ $\text{H}_2 R(1)$ line profiles from photolysis on the $2^1 4^1 \text{ } ^2P_1(1) \sigma \text{H}_2\text{CO}$ line using geometry (b). The top trace is $\text{H}_2(v=0)$ measured on the (3,0) band; the simulated line shape has $\beta_{\text{eff}} = 0.09$ and $v = 1.66 \times 10^6$ cm/s. The middle trace is $\text{H}_2(v=1)$ measured on the (3,1) band, $\beta_{\text{eff}} = 0.04$ and $v = 1.55 \times 10^6$ cm/s. The bottom trace is $\text{H}_2(v=3)$ measured on the (0,3) band; $\beta_{\text{eff}} = -0.18$ and $v = 1.28 \times 10^6$ cm/s. The three peaks are not drawn on the same scale.

ment, S is the product of the absorption Hönl–London and the J dependent Franck–Condon factors,³¹ ν is the H_2 excitation frequency, G accounts for experimental geometry differences (laser beam overlap, H_2CO fluorescence detection, etc.), and b_0 and b_1 are calculated constants for a given rovibrational transition and geometry.^{25,29} The intensity is corrected for the wavelength dependent LiF beamsplitter reflectivity and VUV normalization photomultiplier tube (PMT) response. The correction varies by 20% between 110–116 nm and is constant between 127–129 nm. The intensity is also corrected for the H_2 fluorescence detection sensitivity, which includes emission Franck–Condon and Hönl–London factors, VUV filters, and VUV PMT response as a function of wavelength. For a given H_2 vibrational state, the correction varies by less than 20%.

For a given geometry, the ratio b_1/b_0 is similar for P and R branches. This necessitates the use of multiple geometries to accurately measure the H_2 alignment when probing the $B^1\Sigma_u^+ \leftarrow X^1\Sigma_g^+$ transition. When the geometry is changed, it is very difficult to align the laser beams and detectors precisely as they were. This causes slight H_2 LIF intensity changes which may be misinterpreted as alignment. It is necessary to have a geometry calibration factor which normalizes out the intensity variations caused by experimental changes. $\text{H}_2(J=0)$ has no alignment ($A_0^{(2)} = 0$) and the $R(0)$ LIF intensity reflects this geometry factor G

$$G = \frac{I_{R(0)}}{N_{\text{H}_2\text{CO}}^*}, \quad (4)$$

where $I_{R(0)}$ is the VUV normalized LIF intensity for an $R(0)$ line and $N_{\text{H}_2\text{CO}}^*$ is the $\text{H}_2\text{CO}(S_1)$ number density. The $\text{H}_2\text{CO}(S_1)$ number density is proportional to the H_2CO fluorescence. The effect of photolysis polarization on the H_2CO emission intensity must be considered for the different experimental geometries and excitation lines. If saturation effects are ignored and an isotropic distribution of H_2CO molecules is assumed, the fluorescence intensity $I_{\text{H}_2\text{CO}}$ is given by Eq. (13) of Ref. 29,

$$I_{\text{H}_2\text{CO}} = CN_{\text{H}_2\text{CO}}^* S_{\text{abs}} \sum S_{\text{em}} \left[\frac{1}{9(2J_i + 1)(2J_e + 1)} + \frac{2(-1)^{J_i - J_f} \begin{Bmatrix} J_e & J_e & 2 \\ 1 & 1 & J_f \end{Bmatrix} \begin{Bmatrix} J_e & J_e & 2 \\ 1 & 1 & J_i \end{Bmatrix}}{3(2J_i + 1)} \right] \times P_2(\cos \chi_{\text{ad}}) = CN_{\text{H}_2\text{CO}}^* B_0, \quad (5)$$

where C is a constant, $N_{\text{H}_2\text{CO}}^*$ is proportional to the $\text{H}_2\text{CO}(S_1)$ number density, χ_{ad} is the angle between the absorption and detection polarization axes, S_{abs} and S_{em} are the absorption and emission transition line strengths, J_i , J_e , and J_f are the angular momentum quantum numbers for the initial, excited, and final state of the H_2CO , and the sum is over the detection polarization axes and all allowed emission branches. For the ${}^pP_1(1)o$ H_2CO transition, the fluorescence is isotropic and B_0 is independent of geometry and is equal to 0.0741. For the ${}^rR_0(0)e$ H_2CO transition, B_0 varies with geometry: $B_0 = 0.2667$ when the fluorescence detection direction is perpendicular to ϵ_{phot} [Fig. 2(a)], and $B_0 = 0.1333$ when the fluorescence detection direction is parallel to ϵ_{phot} [Figs. 2(b) and 2(c)]. For these two H_2CO absorption lines, saturation does not reduce the polarization of the fluorescence. The effect of saturation on the fluorescence polarization comes about by changing the ground state m -level distribution, i.e., certain m states are bleached more than others.³² For the ${}^rR_0(0)e$ line, there is only the $m = 0$ ground state level. For the ${}^pP_1(1)o$ line, $J_e = 0$, and the fluorescence must be isotropic regardless of excitation laser intensity.

When the H_2CO fluorescence polarization effects are included, G is expressed as

$$G \propto \frac{I_R(0)}{(I_{\text{H}_2\text{CO}}/B_0)}. \quad (6)$$

The $R(0)$ line is measured 6–10 times for each geometry to accurately determine G ratios for the different geometries.

The $\text{H}_2(v, J)$ populations and alignments are determined from the least squares fit line to the plot of $I/(S\nu G b_0)$ vs $5b_1/4b_0$ which yields an intercept equal to $C_{\text{H}_2}(J'')$ and a slope equal to $A_0^{(2)}C_{\text{H}_2}(J'')$ [see Eq. (3)]. Figure 4 shows this plot for $\text{H}_2(v = 3, J = 1)$ and $\text{H}_2(v = 3, J = 2)$ produced from $2^14^1 S_1$ H_2CO photolysis. Table I lists all of the product H_2 alignments measured in these experiments: H_2

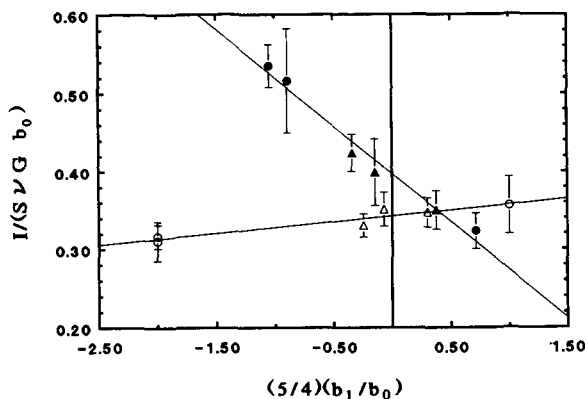


FIG. 4. Alignment plot. The open points are normalized intensities for $\text{H}_2(v = 3, J = 1)$ and the solid points are for $\text{H}_2(v = 3, J = 2)$; circles and triangles are P and R branch intensities. For $\text{H}_2(v = 3, J = 1)$, $C_{\text{H}_2} = 0.34 \pm 0.03$ and $A_0^{(2)} = 0.04 \pm 0.04$; for $\text{H}_2(v = 3, J = 2)$, $C_{\text{H}_2} = 0.40 \pm 0.03$ and $A_0^{(2)} = -0.31 \pm 0.06$. Both measurements are for $2^14^1 S_1$ H_2CO photolysis; photolysis is on the ${}^pP_1(1)o$ and the ${}^rR_0(0)e$ line for $J = 1$ and $J = 2$ H_2 , respectively. The error bars on the data points are ± 2 standard deviations.

($v = 1$) from 4^3 and $2^14^1 S_1$ H_2CO photolysis, and $\text{H}_2(v = 3)$ from $2^14^1 S_1$ H_2CO .

The measured rotational distributions are shown in Table II. For a given vibrational state and photolysis, the *ortho* and *para* J_{H_2} distributions have been normalized to add to 100% since they are produced in separate experiments. The $\text{H}_2(v = 1)$ rotational distributions for 4^3 and 2^14^1 photolysis are shown in Fig. 5. The rotational distributions for the two different vibrational states of $\text{H}_2\text{CO}(S_1)$ are the same within the error bars of the data. Preliminary data for 2^14^3 photolysis gives $\text{H}_2(v = 1)$ rotational distributions which are similar to those of 4^3 and 2^14^1 , peaking in $J = 3-4$.

The $\text{H}_2(v = 1)$ rotational distribution from 4^1 photolysis was not measured because a large VUV background obscured the H_2 fluorescence. $4^1 S_1$ H_2CO has a long lifetime ($0.6 < \tau < 4.7 \mu\text{s}$),³³ and it appears that the excited H_2CO absorbs a 110–116 nm VUV photon and then either fluoresces in the VUV or dissociates to form electronically excited

TABLE I. H_2 alignment $A_0^{(2)}$ from photodissociation of H_2CO .^a

J	4^3		2^14^1	
	$\text{H}_2(v = 1)$	$\text{H}_2(v = 1)$	$\text{H}_2(v = 1)$	$\text{H}_2(v = 3)$
${}^pP_1(1)o\text{H}_2\text{CO}$				
1	0.00 ± 0.07	0.05 ± 0.06	0.04 ± 0.04	
3	0.05 ± 0.07	0.17 ± 0.07	0.06 ± 0.04	
5	0.10 ± 0.16		0.05 ± 0.05	
7	0.08 ± 0.16		0.03 ± 0.11	
${}^rR_0(0)e\text{H}_2\text{CO}$				
2	-0.05 ± 0.06	-0.15 ± 0.07	-0.31 ± 0.06	
4	-0.11 ± 0.08	-0.11 ± 0.07	-0.20 ± 0.09	
6	-0.24 ± 0.11	-0.14 ± 0.11	-0.21 ± 0.13	

^aThe error bars are determined by the extreme maximum and minimum sloped lines that fit the data points plus error bars in the alignment plots.

TABLE II. H_2 rotational distributions from photodissociation of H_2CO .^a

H_2 State		Population			
v	J	4^{1b}	4^{3c}	2^14^{1c}	2^14^{1d}
1	0		0.08 ± 0.01	0.10 ± 0.01	
	1		0.30 ± 0.03	0.27 ± 0.02	0.20
	2		0.32 ± 0.02	0.32 ± 0.02	
	3		0.37 ± 0.03	0.41 ± 0.02	0.26
	4		0.35 ± 0.03	0.37 ± 0.02	
	5		0.18 ± 0.02	0.20 ± 0.02	0.31
	6		0.16 ± 0.01	0.16 ± 0.01	
	7		0.10 ± 0.01	0.10 ± 0.01	0.19
	8		0.06 ± 0.01	0.06 ± 0.02	
	9		0.03	0.02	0.04
3	0			0.10 ± 0.01	
	1	0.30 ± 0.02		0.34 ± 0.03	0.27
	2			0.40 ± 0.03	
	3	0.41 ± 0.03		0.42 ± 0.03	0.30
	4			0.32 ± 0.02	
	5	0.21 ± 0.02		0.18 ± 0.02	0.29
	6			0.15 ± 0.01	
	7	0.08 ± 0.02		0.06 ± 0.01	0.14
	8			0.04	

^aThe *ortho* and *para* distributions each sum up to 1.0 as they are measured in separate experiments on different photolysis excitation transitions.

^bPhotolysis on the unresolved ${}^1R_1(1)e + o$ lines. The alignment was not measured and is assumed to be zero. The error bars are ± 2 standard deviations of the mean.

^c*ortho* photolysis is on the ${}^1P_1(1)o$ line. *Para* photolysis is on the ${}^1R_0(0)e$ line. The error bars are determined by the extreme maximum and minimum line intercepts that fit the data points plus error bars in the alignment plots.

^dCARS data from Ref. 4.

products that fluoresce in the VUV.³⁴ This interference does not exist at the longer VUV wavelengths (127–129 nm) used to probe H_2 ($v = 3$).

Figure 6 shows the H_2 ($v = 3$) rotational distributions from 4^1 and $2^14^1 S_1$ H_2CO . The 4^1 photolysis was on the unresolved ${}^1R_1(1)e + o$ line, because it was the only photolysis line that produced enough product to adequately measure a population. The alignment was not measured and is neglected in determining the rotational population. For $2^14^1 S_1$ H_2CO , the *ortho* distribution is from photolysis of the ${}^1P_1(1)o$ line while the *para* distribution is from the ${}^1R_0(0)e$ line. The two S_1 vibrational states produce very similar H_2 ($v = 3$) J distributions.

Figure 7 is the Boltzmann plot for the $2^14^1 S_1$ H_2CO photolysis rotational distributions. The rotational distributions can be described by a temperature: $T = 1730 \pm 170$ K for H_2 ($v = 1$) and $T = 1240 \pm 80$ K for H_2 ($v = 3$).

B. Product quantum state correlations

The average velocity for a particular H_2 (v, J) state is determined from the H_2 maximum Doppler shift, $\Delta\nu_D$. The corresponding CO average velocity and the total average translational energy in the products is calculated using conservation of linear momentum. Tables III and IV list the measured average velocities. A translational energy histo-

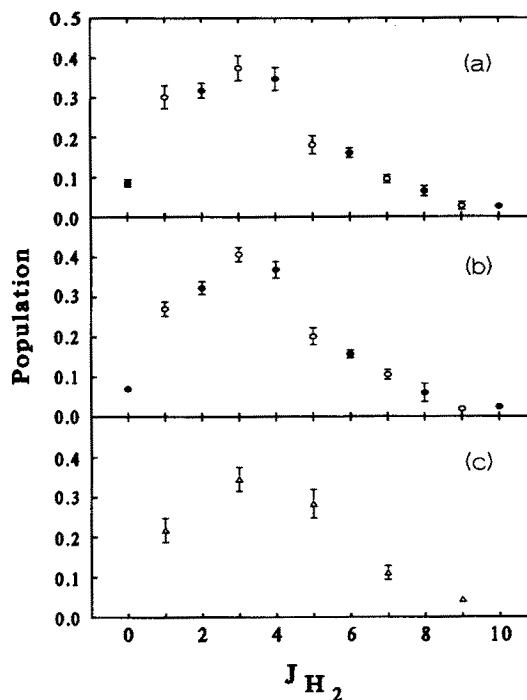


FIG. 5. H_2 ($v = 1$) rotational distributions. (a) 4^3 and (b) $2^14^1 S_1$ H_2CO photolysis: *para* H_2 (solid circles) is from photolysis on the ${}^1R_0(0)e$ H_2CO line and *ortho* H_2 (open circles) is from photolysis on the ${}^1P_1(1)o$ H_2CO line. (c) Photolysis is on the unresolved ${}^1R_0(1)e + o$ lines of $2^14^1 S_1$ H_2CO .

gram is constructed by combining the measured average product translational energy for each H_2 (v, J) with the relative population for that state. The vibrational distribution is from the CARS work,⁴ and the rotational distributions for H_2 ($v = 0$) and H_2 ($v = 2$) are estimated to be the same as the H_2 ($v = 1$) measured distribution. Figure 8 compares

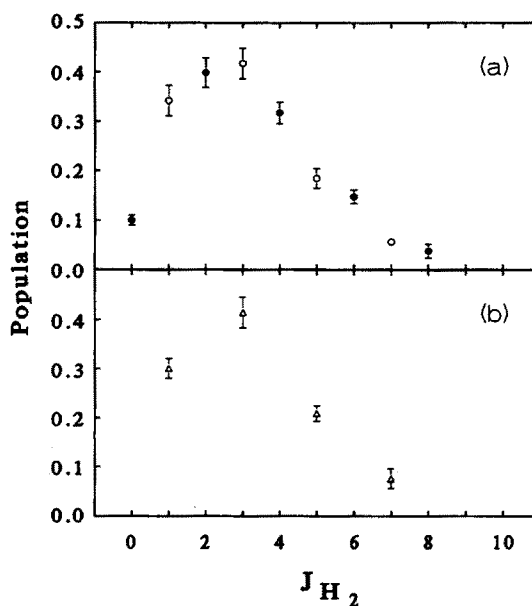


FIG. 6. H_2 ($v = 3$) rotational distributions. (a) $2^14^1 S_1$ H_2CO : *para* H_2 (solid circles) is from photolysis on the ${}^1R_0(0)e$ H_2CO line and *ortho* H_2 (open circles) is from photolysis on the ${}^1P_1(1)o$ H_2CO line. (b) Photolysis on the unresolved ${}^1R_0(1)e + o$ lines of $4^1 S_1$ H_2CO .

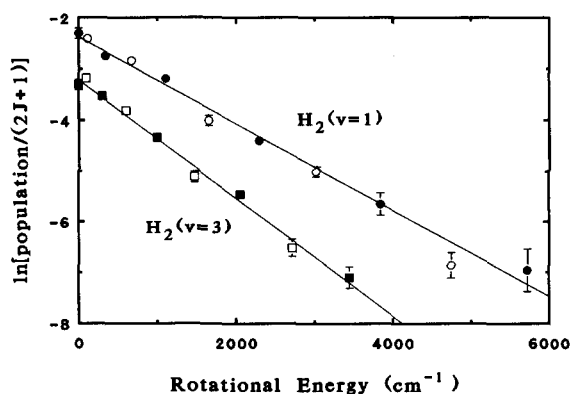


FIG. 7. H_2 rotational distribution Boltzmann plot for $2^1 4^1 S_1$ H_2 CO photolysis. *Para* H_2 (solid symbols) is from photolysis on the $^2R_0(0)e$ H_2 CO line and *ortho* H_2 (open symbols) is from photolysis on the $^2P_1(1)o$ H_2 CO line. The lines drawn are the weighted least squares fit to the combined *ortho* and *para* points and correspond to $T = 1730 \pm 170$ K for $H_2(v=1)$ and $T = 1240 \pm 80$ K for $H_2(v=3)$. The plots have been displaced one unit on the abscissa for clarity.

the histogram of the translational energies obtained from the average $H_2(v, J)$ velocities measured for photolysis on the $2^1 4^1$ $^2R_0(0)e$ and $^2P_1(1)o$ lines with the product translational energy distribution measured by time-of-flight mass spectroscopy.¹⁰ In the graph, the translational energy histogram is normalized so that if translational energies for all of the $H_2(v, J)$ states had been measured, the total area would be unity. The paucity of intensity in the $H_2(v=0)$ and $H_2(v=2)$ areas is because velocities were measured for only a few rota-

tional states of those vibrational states. The time-of-flight translational energy distribution is also normalized to unit area. The agreement between the time-of-flight data and the H_2 velocities is very good. There is a correlation between the translational energy of the products and the internal energy of the H_2 : lower translational energies correspond to H_2 with higher internal energy.

The average CO rotational state that corresponds to a given $H_2(v, J)$ state is determined by conservation of energy:

$$\begin{aligned} E_{\text{rot}}(\text{CO}) &= BJ(J+1) - D_0 J^2(J+1)^2 \\ &= E_{\text{avl}} - E_{\text{int}}[H_2(v, J)] \\ &\quad - E_{\text{trans}}(H_2 + \text{CO}), \end{aligned} \quad (7)$$

where B and D_0 are CO($v=0$) rotational constants, E_{int} is the rovibrational energy of the H_2 product, and E_{trans} is the total translational energy of the products. E_{avl} is the total energy available to the products

$$E_{\text{avl}} = E_{\text{Rot}}(H_2\text{CO}) + h\nu - \Delta H(0 \text{ K}), \quad (8)$$

where $E_{\text{Rot}}(H_2\text{CO})$ is the $H_2\text{CO}(S_0)$ rotational energy, $h\nu$ is the photolysis photon energy, and $\Delta H(0 \text{ K})$ is the heat of the reaction, $\Delta H(0 \text{ K}) = -2.17 \pm 0.11$ kcal/mol.^{35,36} The CO is considered to be in its ground vibrational state—experimentally only 12% is measured in $v=1$ for $2^1 4^1 S_1$ $H_2\text{CO}$ photolysis.^{2,3} Tables III and IV list the product correlation results. Figure 9 shows the histogram of the J_{CO} distribution obtained from the measured H_2 average velocities from photolysis on the $2^1 4^1$ $^2R_0(0)e$ and $^2P_1(1)o$ lines.³⁷ This figure is constructed in the same manner as Fig. 8. As pre-

TABLE III. $2^1 4^1 S_1$ $H_2\text{CO}$ product correlations and impact parameters.

H ₂ state		Average H ₂ velocity (10 ⁶ cm s ⁻¹)	$\langle J_{\text{CO}} \rangle$	Impact parameter ^a (Å)		
<i>v</i>	<i>J</i>			$J_{\text{CO}} + J_{\text{H}}$	J_{CO}	$J_{\text{CO}} - J_{\text{H}}$
<i>^2R_0(0)e</i> photolysis						
0	2	1.65	51.3 ± 3.8	1.03	0.99	0.96
1	0	1.57 ± 0.01 ^b	45.4 ± 1.6	0.93	0.93 ± 0.04	0.93
	2	1.58	42.2	0.90	0.86	0.82
	4	1.55	42.9	0.97	0.89	0.81
	6	1.52	40.3	0.98	0.85	0.73
2	2	1.42 ± .03	44.5 ± 4.4	1.05	1.00	0.96
	4	1.42	39.1	0.97	0.88	0.79
	6	1.41	33.6	0.90	0.77	0.63
3	0	1.35 ± 0.02	32.7 ± 2.1	0.78	0.78 ± 0.06	0.78
	2	1.30	39.1 ± 1.5	1.01	0.96	0.92
	4	1.29	35.7	0.99	0.89	0.79
	6	1.26	33.2	1.00	0.85	0.70
<i>^2P_1(1)o</i> photolysis						
0	1	1.66 ± 0.02	53.5 ± 3.4	1.05	1.03	1.01
	5	1.64	47.8	1.03	0.93	0.84
	7	1.60	46.2	1.06	0.92	0.79
1	1	1.55 ± 0.01	48.6 ± 1.6	1.02	1.00 ± 0.04	0.98
	3	1.50	51.5	1.16	1.10	1.03
	5	1.49	47.9	1.14	1.03	0.92
	7	1.46	45.0	1.14	0.99	0.84
3	1	1.28 ± 0.01	44.0 ± 1.4	1.13	1.10 ± 0.04	1.08
	3	1.26	42.8	1.16	1.09	1.01
	5	1.23	41.8	1.22	1.09	0.96

^aThe H_2 and CO J vector combinations correspond to corotation $L = (J_{\text{CO}} + J_{\text{H}})$, counterrotation $L = (J_{\text{CO}} - J_{\text{H}})$, and $L = J_{\text{CO}}$.

^bThe error bars represent ± 2 standard deviations of the mean.

TABLE IV. $4^3 S_1$ H_2CO product correlations and impact parameters.

H ₂ state		Average H ₂ velocity (10 ⁶ cm s ⁻¹)	$\langle J_{CO} \rangle$	Impact parameter ^a (Å)		
ν	J			$J_{CO} + J_{H_2}$	J_{CO}	$J_{CO} - J_{H_2}$
<i>^rR₀(0)e</i> photolysis						
1	0	1.58 ± 0.01 ^b	41.0 ± 1.2	0.83	0.83 ± 0.03	0.83
	2	1.56	43.5	0.93	0.89	0.85
	4	1.53	42.5	0.97	0.89	0.81
	6	1.50	40.5	0.99	0.86	0.74
<i>^pP₁(1)p</i> photolysis						
1	1	1.58 ± 0.01	41.0 ± 1.6	0.85	0.83 ± 0.04	0.81
	3	1.56	41.0	0.90	0.84	0.78
	5	1.54	38.2	0.90	0.80	0.69
	7	1.50	36.4	0.93	0.78	0.63

^aThe H₂ and CO J vector combinations correspond to corotation $L = (J_{CO} + J_{H_2})$, counter-rotation $L = (J_{CO} - J_{H_2})$, and $L = J_{CO}$.

^bThe error bars represent ± 2 standard deviations of the mean.

viously predicted,⁴ higher vibrational states of H₂ are correlated with lower rotational states of CO.

IV. DISCUSSION OF RESULTS

A. Product H₂ alignment

The method used in this work to measure alignments is prone to systematic errors, so it is useful to have a check. The product alignment from *^pP₁(1)o* photolysis should be zero because the excited state parent molecule has $J = 0$ and, therefore, its wave function is isotropic. Table I shows that most of the alignments measured for this photolysis are near zero, though slightly positive. One problem is the *^pP₁(1)o* H₂CO line is not resolved from the *^pQ₁(3)e* line. At the measured H₂CO rotational temperature of 5 K, photolysis of the *^pQ₁(3)e* line accounts for 10% of the products; if $T = 8$ K, this increases to 26%. The *^pQ₁(3)e* line may account for the small systematic positive alignments measured for the *^pP₁(1)o* photolysis. Another source of systematic error might be an alignment of the ground state H₂CO(1₁₁) by

collisions with helium in the supersonic expansion. This would affect our method of using the H₂CO(S_1) fluorescence to normalize for photolysis laser power and H₂CO number density. This can be avoided by using data from geometries (b) and (c) only, but it results in large alignment uncertainties.

Ortho H₂ has nuclear spin $I = 1$ which might cause hyperfine depolarization of the observed alignment. The nuclear spin I of a product couples with J to form a resultant F . The precession of I and J around F can depolarize the alignment; i.e., the observed alignment can be smaller than the nascent alignment.^{25,29,30} In general, if the frequency splitting ω_{if} between two hyperfine levels is much less than $1/\tau$, where τ is the time available for the depolarization to occur, the depolarization is negligible. The hyperfine splitting for the H₂ $X^1\Sigma_g^+$ state is 550 kHz,³⁸ and the product H₂ is probed up to 100 ns after being born. This is not quite in the $\omega_{if} \ll 1/\tau$ limit, and Eq. (37) of Ref. 30 is used to calculate the effect of depolarization on the alignment measurements. For $J = 1$, the measured alignment is 87% of the nascent alignment when the time between the photolysis and probe laser

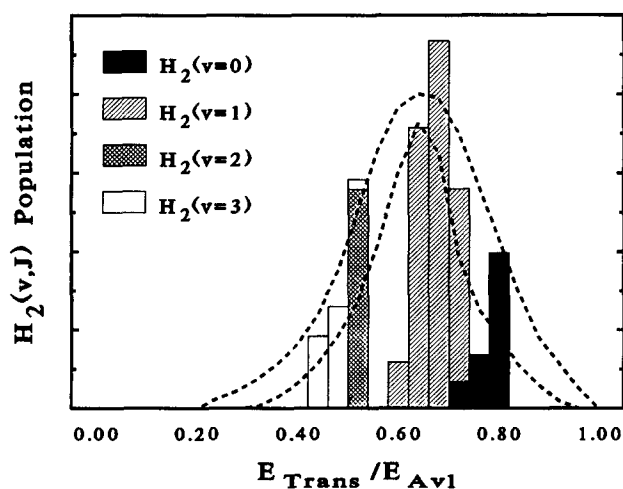


FIG. 8. Histogram of the product translational energies calculated from the H₂(ν, J) average velocities and populations measured for $2^1 4^1$ *^pP₁(1)o* and *^rR₀(0)e* H₂CO photolyses. The dashed lines are the upper and lower limits on the measured translational energy distribution from Ref. 10.

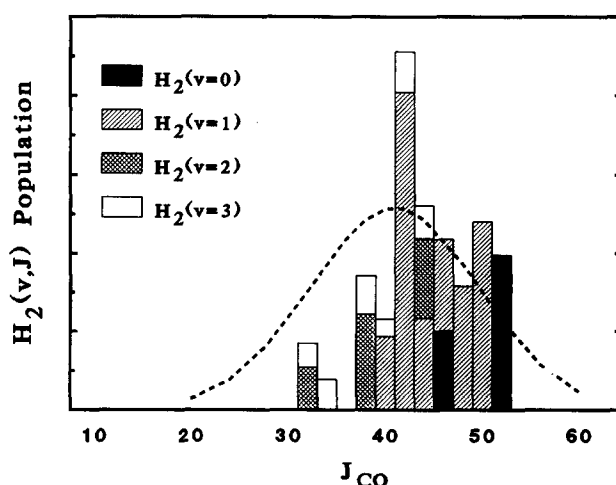


FIG. 9. Histogram of the J_{CO} calculated from the H₂(ν, J) average velocities and populations measured for $2^1 4^1$ *^pP₁(1)o* and *^rR₀(0)e* H₂CO photolyses. The dashed line is the measured J_{CO} distribution from Ref. 3.

pulses is 100 ns. For $J \geq 5$, the measured alignment is within 1% of the nascent alignment.

The nuclear spin depolarization can also have an effect on the product fluorescence polarization. The hyperfine splitting for the $B^1\Sigma_u^+$ state is unknown, but if it is similar to the $X^1\Sigma_g^+$ state, the 1 ns fluorescence lifetime is short compared to the hyperfine precessional period and depolarization from nuclear spin can be neglected. The alignment values in Table I are measured alignments, and the small effects from nuclear spin depolarization are neglected. For *para* H_2 , $I = 0$ and there is no hyperfine depolarization.

The alignments measured for the ${}^1R_0(0)e$ photolysis are negative, and in some cases fairly large (Table I). The range of possible values for prompt dissociation are $-0.4 < A_0^{(2)} < 0.8$ for products in the high J limit. For products with low J , the ranges are slightly greater: e.g., for $J = 1$, $-1.0 < A_0^{(2)} < 0.5$, and for $J = 2$, $-0.7 < A_0^{(2)} < 0.7$.³⁰ The alignment is not completely washed out by rotation during the long lifetime of the excited state parent molecule [$2^14^1S_1 H_2CO(J' = 1, K'_a = 1, K'_c = 1)\tau \approx 70$ ns] which agrees qualitatively with the Nagata *et al.* theoretical treatment of parent rotation effects on fragment alignment.³⁹ The alignments measured here are outside the allowed limits of their theory, but their approximations of $J_{\text{fragment}} \gg J_{\text{parent}} \gg 0$ are not valid in this experiment. The negative alignment is consistent with the *ab initio* transition state and reaction coordinate for these type *B* band photolyses, where the transition dipole is in the plane of the molecule and perpendicular to the CO bond.

B. Rotational populations

The H_2 rotational populations measured by LIF agree reasonably well with the previous CARS work.⁴ A comparison of the LIF and CARS rotational distributions is given in Table II. The LIF distribution in $v = 1$ peaks between $J = 3$ and 4 which is lower than the $J = 5$ peak found in the CARS experiments. This suggests that the collisional cooling of translation in the CARS experiment produced a small rotational heating. Both methods agree that the rotational distribution in $v = 3$ is slightly cooler than that of $v = 1$.

Table V lists the average rotational energies for the measured distributions. There appears to be no evidence for influence of the $H_2CO(S_1)$ vibrational state on the H_2 rota-

tional distribution. This supports the suggestion that the H_2 distributions are determined by the potential surface at the transition state and not the excited H_2CO surface. The difference in energy between the 4^3 and 2^14^1 bands is only 360 cm^{-1} (while that between 4^1 and 2^14^1 is 1180 cm^{-1}). This extra energy could at most shift the peak of the rotational distribution by one unit of rotational angular momentum. Since the energy effect is small, any measurable differences in the populations might be the result of coupling between the H_2 populations and parent vibrational motions. There is no evidence for this coupling. It is likely that the $H_2CO(S_0^*)$ vibrational modes are highly mixed and that internal conversion gives vibrationally randomized molecules.⁴⁰ It is therefore not surprising that the product distributions are insensitive to the initial parent state. Although the populations seem independent of the initial $H_2CO(S_1)$ vibrational state, there is evidence that the vector correlations differ for 4^3 and 2^14^1 excitation.^{27,28}

The H_2 rotational distribution may be correlated with the initial $H_2CO(S_1)$ rotational state. Excitation on the unresolved ${}^1R_1(1)e + o$ ($J' = K'_a = 2$) and ${}^2P_1(1)o$ ($J' = K'_a = 0$) differs by two units of angular momenta and only 37 cm^{-1} in energy. The average rotational energy for the $H_2(v = 1)$ distribution from ${}^1R_1(1)e + o$ photolysis is 200 cm^{-1} greater than that from ${}^2P_1(1)o$ photolysis. This may be caused by coupling of the parent rotation to the product H_2 rotation. Unfortunately, there are limited H_2CO J and K_a states in the molecular free jet, so that a broader J range was not studied.

C. Product quantum state correlations

The measured product state correlations show a striking dependence of the CO J state on the H_2 vibrational state (Table III). As more of the available energy is put into H_2 vibration, the CO rotational energy decreases. The correlation of product quantum states was predicted in previous H_2CO studies.⁴ The CO rotational distribution is highly inverted and best explained in terms of a large dissociation impact parameter ($0.8\text{--}0.9 \text{ \AA}$).³ Constraining the impact parameter distribution about some large value produces the observed correlation as follows. Conservation of angular momentum requires that

$$\mathbf{j}_{\text{tot}} = \mathbf{j}_{H_2CO} = \mathbf{L} + \mathbf{j}_{CO} + \mathbf{j}_{H_2}, \quad (9)$$

TABLE V. Average H_2 rotational energies^a and rotational quantum numbers.

H ₂ CO photolysis				$\langle E_{\text{rot}} \rangle$		$\langle J \rangle$	
S ₁ vib.	J'	K' _a	E _{av}	H ₂ (v = 1)	H ₂ (v = 3)	H ₂ (v = 1)	H ₂ (v = 3)
4 ¹	${}^1R_1(1)e + o$	2	2	29 109			
4 ³	${}^2P_1(1)o$	0	0	29 895	1020 ± 25	800 ± 32	3.12 ± 0.10
	${}^1R_0(0)e$	1	1	29 904	1240		3.28 ± 0.08
2 ¹ 4 ¹	${}^2P_1(1)o$	0	0	30 254	1040 ± 25	710 ± 22	2.92 ± 0.08
	${}^1R_0(0)e$	1	1	30 264	1210	870	3.38
	${}^1R_1(1)e + o$	2	2	30 291	1270		3.76
	CARS ^b				1470	1020	3.84
							4.22
							3.60

^aEnergies in cm^{-1} .

^bReference 4. Initial $2^14^1S_1$ rotational states include $J = 5\text{--}15$ and $K_a = 0, 2$.

where L is the orbital angular momentum of the separating products and the j 's are rotational vectors. The initial parent angular momentum is essentially zero ($J_{\text{H}_2\text{CO}} = 0$ or 1) so that

$$L = \mu v b \approx |j_{\text{CO}} + j_{\text{H}_2}|, \quad (10)$$

where μ is the H_2 -CO reduced mass, v is the relative velocity of the products, and b is the impact parameter. Most of the internal angular momentum of the products is in j_{CO} . As more energy is put into internal product excitation, the translational energy and therefore the velocity v must decrease. Since b is constrained, a lower velocity results in less orbital angular momentum and therefore less CO rotational angular momentum. The constrained impact parameter causes internally excited H_2 states to correlate with CO states in lower rotational levels.

The average impact parameter can be calculated from the product correlation data using Eq. (10). In order to do so, however, some assumption must be made about the relation of the H_2 and CO rotation vectors. The impact parameter as a function of J_{H_2} is given in Tables III and IV for several combinations of these vectors. The limiting cases are j_{H_2} parallel to j_{CO} (corotation) and j_{H_2} antiparallel to j_{CO} (counterrotation). As suggested by the v - J correlation, the situation may be intermediate between the parallel and antiparallel extremes due to the nonplanar motions of the transition state.²⁷ At this time, the experimental evidence does not discriminate between corotation or counterrotation, though the deviations in the impact parameters derived are smaller for corotation or $L = J_{\text{CO}}$ than for counterrotation. The only firm conclusion is that the calculated impact parameters are large and well outside the center of the carbon nucleus as previously suggested.

In the $2^1A'$ photolyses (Table III), there is evidence that the J_{CO} produced from photolysis on the $^3P_1(1)O$ line is 6-7 quanta greater than the J_{CO} from photolysis on the $^1R_0(0)e$ line and that the impact parameters for the two photolyses differ by about 0.2 Å. This may be an artifact. The two photolyses have different product anisotropies which results in different H_2 line shapes²⁸: in general, the *para* lines are "more round" than the *ortho* lines. These different line shapes may cause a systematic error in determining the average H_2 velocities. However, $P(1)$ lines, which are round, give the same velocities as $R(1)$ lines, which are square.⁴¹ Work is in progress to measure the J_{CO} distributions from these two photolyses directly.

V. PRODUCT STATE DISTRIBUTION MODELS

The most surprising aspect of these results is further evidence of the Boltzmann nature of the H_2 rotational distributions. No other aspect of the dissociation product distributions has Boltzmann-like character. The CO rotational distribution is peaked at large J and the H_2 vibrational distribution is inverted. There is a strong dynamical preference to put energy into H_2 translation. Although the H_2 rotational distributions can be expressed in terms of a rotational temperature, the release of energy into H_2 degrees of freedom is certainly not statistical. Prior distributions, where energy is partitioned by a density of states approach constrained only

by total available energy,⁴² poorly predict the energy distribution.⁴³ The calculated H_2 prior distribution peaks in $v = 0, J = 9$. Phase space theory,^{44,45} which includes angular momentum constraints, also overestimates the rotational excitation found in H_2 (peaking in $v = 0, J = 12$).

A. Trajectory calculations

Population distributions have been calculated from semiclassical trajectory calculations on the Handy and Carter H_2CO potential surface.⁴⁶ A normal mode analysis of the *ab initio* transition state is performed using the calculated force constants for the DZ SCF optimized geometry of Goddard and Schaefer.⁶ The normal modes and frequencies are shown in Fig. 10.⁴⁷

The initial conditions of the trajectories are chosen from random zero-point positions and momenta in each of the five bound normal modes on the ground state surface at the transition state. Since the photon energy is larger than the transition state's potential energy,⁴⁸ this excess energy is put into momentum along the reaction coordinate. The trajectories are then propagated using a fifth order Adam-Moulson integrator with variable step size⁴⁹ until the H_2 and CO products are separated by 10 Å.

The final product states are semiclassically binned following each trajectory. The rotational quantum number J is calculated from the classical angular momentum in each species. The angular momentum j is given by

$$j = |\mathbf{r} \times \mathbf{p}| = \hbar [J(J+1)]^{1/2} \quad (11)$$

from which J is determined. The CO vibrations are binned using the Bohr Sommerfeld rule by integrating from one turning point to the other. The H_2 vibrational energy is determined from conservation of energy and then assigned a vibrational quantum number.

The trajectory calculations do not reproduce the experimental distributions well. The CO distribution peaks in $v = 0, J = 20$ while the H_2 distribution peaks in $v = 0, J = 5$. This is most likely due to the potential surface, which has

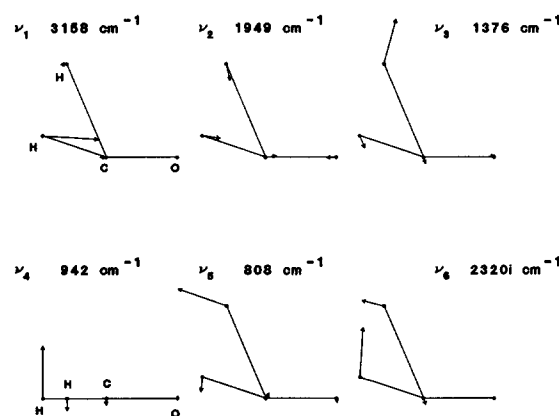


FIG. 10. *Ab initio* $\text{H}_2\text{CO} \rightarrow \text{H}_2 + \text{CO}$ transition state normal modes and frequencies corresponding to the calculated force constants for the DZ SCF optimized geometry of Ref. 6. The out-of-plane bend is ν_4 . The reaction coordinate is ν_6 and is shown directed towards the products.

been fit to the H_2CO ground state well and adjusted for the transition state geometry and energy. Presently, Lester's group is working to improve the surface near the transition state and along the reaction coordinate for future scattering calculations.

B. Impulsive model

The modified impulsive model⁵⁰ as applied to a planar tetra-atomic is combined with the vibrational motions of the parent molecule to model the H_2 and CO rotational distributions and the H_2/CO product quantum state correlations. This is a reasonable model since the exit valley is highly repulsive and both the H_2 and CO vibrations are "stiff." Because H_2CO is predissociative, the transition state geometry is used, instead of the traditional ground state geometry appropriate for direct dissociations.

The normal modified impulsive model is applicable for triatomics and restricts the impulse to be along the breaking bond. For H_2CO , the model is changed to include four atoms in a plane, and the impulse is not required to be along bonds. The impulse is applied between a point along the H-H line and a point along the CO line outside of the C nucleus. Figure 11 shows the relevant parameters. The parameter x_{CO} is a fixed distance from the C nucleus along the line defined by the CO axis. It is a variable that directly determines the peak of the calculated CO rotational distribution. The parameter x_{H_2} is a fixed distance from the H-H center of mass along the H-H axis. The energy available to be partitioned between product rotation and product translation is E'_{avl} and is equal to the total energy available to the products minus the vibrational energy of the products. With this definition of E'_{avl} , the energy that is partitioned into CO rotation is

$$E_{\text{CO}}^{\text{rot}} = \frac{E'_{\text{avl}}}{1 + [\mu_{\text{CO}} \tilde{r}_{\text{CO}}^2 / \mu_{\text{H}_2\text{-CO}} b_{\text{CO}}^2] + [\mu_{\text{CO}} \tilde{r}_{\text{CO}}^2 b_{\text{H}_2}^2 / \mu_{\text{H}_2} \tilde{r}_{\text{H}_2}^2 b_{\text{CO}}^2]}, \quad (18)$$

where $\mu_{\text{H}_2\text{-CO}}$ is the reduced mass of $\text{H}_2\text{-CO}$ [$= m_{\text{H}_2} m_{\text{CO}} / (m_{\text{H}_2} + m_{\text{CO}})$]. The H_2 rotational energy is calculated from

$$\begin{aligned} E_{\text{H}_2}^{\text{rot}} / E_{\text{CO}}^{\text{rot}} &= [\mu_{\text{CO}} \tilde{r}_{\text{H}_2}^2 b_{\text{H}_2}^2 / \mu_{\text{H}_2} \tilde{r}_{\text{H}_2}^2 b_{\text{CO}}^2] \\ &= B_{\text{H}_2} b_{\text{H}_2}^2 / B_{\text{CO}} b_{\text{CO}}^2, \end{aligned} \quad (19)$$

where B_{H_2} and B_{CO} are the rotational constants for the appropriate vibrational states of the product H_2 and CO . The magnitude of the CO angular momentum j_{CO} is given by

$$j_{\text{CO}} / \hbar = (E_{\text{CO}}^{\text{rot}} / B_{\text{CO}})^{1/2} \quad (20)$$

and the H_2 angular momentum is calculated in a similar manner. The direction of the angular momentum is perpendicular to the plane of the parent. Note that if the impulse is applied to the H_2 center of mass, $b_{\text{H}_2} = 0$, and Eq. (18) reduces to the form appropriate for a triatomic parent, where the H_2 is treated as an atom.

The modified impulse model only gives a single angular momentum for a given E'_{avl} ; it does not account for the

$$E_{\text{CO}}^{\text{rot}} = \frac{E_{\text{CO}}^{\text{rot}} E'_{\text{avl}}}{E_{\text{CO}}^{\text{trans}} + E_{\text{H}_2}^{\text{trans}} + E_{\text{CO}}^{\text{rot}} + E_{\text{H}_2}^{\text{rot}}}. \quad (12)$$

Conservation of linear momentum gives

$$m_{\text{H}_2} v_{\text{H}_2} = m_{\text{CO}} v_{\text{CO}}, \quad (13)$$

where m_{H_2} , m_{CO} , v_{H_2} , and v_{CO} are the masses and final velocities of H_2 and CO . The rotational energy for each diatomic fragment is

$$E_{\text{AB}}^{\text{rot}} = \frac{j_{\text{AB}}^2}{2\mu_{\text{AB}} \tilde{r}_{\text{AB}}^2} = \frac{(m_{\text{AB}} v_{\text{AB}} b_{\text{AB}})^2}{2\mu_{\text{AB}} \tilde{r}_{\text{AB}}^2}, \quad (14)$$

where AB represents H_2 or CO ; the AB angular momentum is j_{AB} , its reduced mass is μ_{AB} , and its average bond length is \tilde{r}_{AB} . The shortest distance from the AB center of mass to the line along the impulsive force is b_{AB} . It is the "effective AB impact parameter" and for CO is given by

$$b_{\text{CO}} = \sin \theta_{\text{CO}} (x_{\text{CO}} + m_0 r_{\text{CO}} / m_{\text{CO}}), \quad (15)$$

where r_{CO} is the CO bond length in the parent and m_0 is the oxygen atom mass. The "effective H_2 impact parameter" b_{H_2} is given by

$$b_{\text{H}_2} = x_{\text{H}_2} \sin \theta_{\text{H}_2}, \quad (16)$$

where θ_{CO} , θ_{H_2} , x_{CO} , and x_{H_2} are defined in Fig. 11(a). The total reaction impact parameter b is equal to $b_{\text{CO}} + b_{\text{H}_2}$ for corotating products and $|b_{\text{CO}} - b_{\text{H}_2}|$ for counterrotating products [Fig. 11(b)]. The translational energy for each fragment is given by

$$E_{\text{AB}}^{\text{trans}} = m_{\text{AB}} v_{\text{AB}}^2 / 2. \quad (17)$$

Substituting Eqs. (13), (14), and (17) into Eq. (12) and simplifying gives

width of rotational distributions. Parent rotational and vibrational motions can transfer angular momentum to the products. A model similar to the one described by Levene and Valentini⁵¹ to calculate rotational distributions from direct photodissociations is used, but here, the fragment angular momentum is affected by the transition state geometry and motions instead of the ground state geometry and motions. Because low J states of $\text{H}_2\text{CO}(S_1)$ are excited in this work, only the effect of parent vibrational motion on the product rotational distribution is considered here, though parent rotation can be included in a straight forward manner.⁵¹ The *ab initio* transition state geometry and normal coordinates are used to describe the parent motions at the time of dissociation. For a given normal coordinate, the momentum of the atoms is either in the plane of the equilibrium geometry or perpendicular to the plane. The angular momentum transferred to either diatomic will likewise be perpendicular to the plane (in-plane normal modes) or in the plane (out-of-plane normal modes).

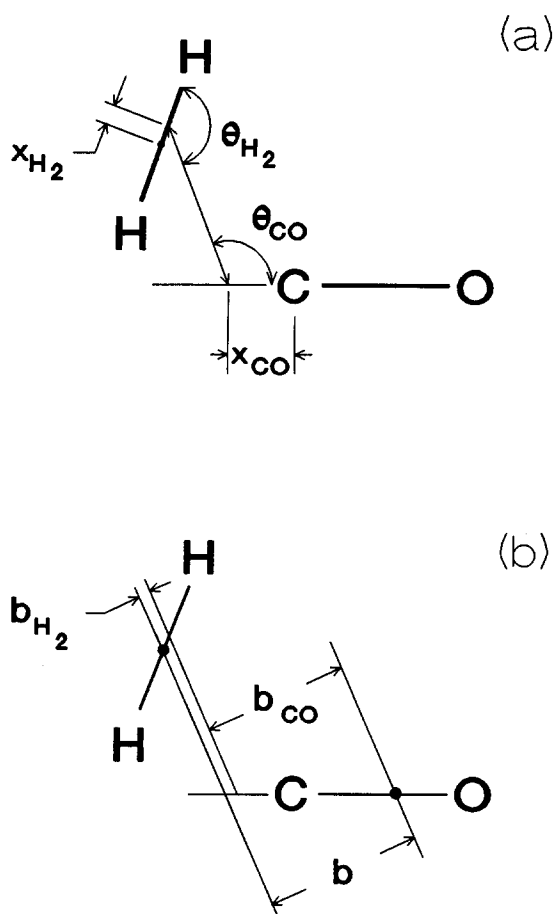


FIG. 11. (a) The parameters used in the semiclassical impulsive model calculation. (b) The effective impact parameters b_{H} , and b_{CO} ; b is the impact parameter for the reaction. The points represent the H-H and CO centers of mass.

The vibrations are treated quantum mechanically and are represented by harmonic oscillator wave functions. The total energy is less than 2000 wave numbers above the zero-point energy of the transition state for dissociation, thus contributions to the rotational distribution widths will be predominantly from parent zero-point motions. Therefore, only zero-point motions are included in the following calculation. The quantum mechanical momentum distribution $P(P_i)dP_i$ for the zero-point motion of mode i is

$$P(P_i)dP_i = \frac{\exp(-P_i^2/P_{\text{max},i}^2)}{(\pi P_{\text{max},i}^2)^{1/2}} dP_i, \quad (21)$$

where P_i is the momentum, and $P_{\text{max},i} = (h\nu_i\mu_i)^{1/2}$ is the classically allowed maximum momentum; μ_i is the reduced mass of normal mode i . For a given mode and phase, the Cartesian components of the linear momentum of each of the four atoms are determined and the corresponding H_2 and CO angular momentum is classically calculated.

For computational simplicity, and to be consistent with the impulsive model developed for a planar tetra-atomic, the geometry is fixed at the planar equilibrium geometry. The effect of geometry changes within the classically allowed turning points of various modes is small. With the fixed geometry approximation, the angular momentum transferred

from the parent to either diatomic reflects the linear momentum distribution. For mode i zero-point motions this is

$$P(j_i)dj_i = \frac{\exp(-j_i^2/j_{\text{max},i}^2)}{(\pi j_{\text{max},i}^2)^{1/2}} dj_i, \quad (22)$$

where j is the angular momentum of the diatomic, and j_{max} is the angular momentum corresponding to the classically allowed linear momentum P_{max} . The angular momentum is either perpendicular to the plane of the parent molecule, or in the plane and perpendicular to the line joining the two atoms of the diatomic.

The five real normal modes have random phases with respect to each other. The diatomic rotational distribution can be calculated by randomly selecting the phases of the five modes, and weighting the corresponding total angular momentum by the probability of being in that part of phase space. This is repeated many times until a suitable sampling of phase space has been accomplished. This is equivalent to numerically evaluating a fifth order integral and is computationally intensive.

A computationally simpler approach is to convolute the angular momentum distributions from the four planar normal modes in the manner appropriate for Gaussian functions. The angular momentum transferred from these modes to the diatomic is perpendicular to the plane of the parent and is denoted j_{\perp} . Then

$$j_{\text{max},\perp}^2 = j_{\text{max},1}^2 + j_{\text{max},2}^2 + j_{\text{max},3}^2 + j_{\text{max},5}^2 \quad (23)$$

and the total j_{\perp} probability function from parent zero-point motions is the same as Eq. (22) with j_{\perp} and $j_{\text{max},\perp}$ replacing j_i and $j_{\text{max},i}$. Inclusion of the angular momentum from the impulsive force j_{imp} which is always perpendicular to the plane of the parent, gives the total j_{\perp} probability function:

$$P(j_{\perp})dj_{\perp} = \frac{\exp[-(j_{\perp} - j_{\text{imp}})^2/j_{\text{max},\perp}^2]}{(\pi j_{\text{max},\perp}^2)^{1/2}} dj_{\perp}. \quad (24)$$

In a similar manner, the parent contributions to the diatomic angular momentum directed in the plane of the parent and perpendicular to the diatomic bond axis is determined. This angular momentum is j_{\parallel} . Only ν_4 contributes, so $j_{\text{max},\parallel} = j_{\text{max},4}$, and the in-plane angular momentum distribution $P(j_{\parallel})dj_{\parallel}$ is similar to Eq. (22).

The total classical angular momentum probability is the product $P(j_{\perp})P(j_{\parallel})dj_{\perp}dj_{\parallel}$. This is most conveniently expressed in polar coordinates, where the plane of the coordinate system is defined by the directions of j_{\perp} and j_{\parallel} . Then

$$p(j)dj = \int_0^{2\pi} \frac{\exp[-(j_{\perp} - j_{\text{imp}})^2/j_{\text{max},\perp}^2 - j_{\parallel}^2/j_{\text{max},\parallel}^2] d\Phi}{\pi j_{\text{max},\perp} j_{\text{max},\parallel}} j dj, \quad (25)$$

where j is the magnitude of the total angular momentum [$j = (j_{\perp}^2 + j_{\parallel}^2)^{1/2}$], $j_{\perp} = j \cos \Phi$, and $j_{\parallel} = j \sin \Phi$. The integral over Φ is numerically evaluated and $P(j)$ is converted to a quantum distribution by binning into the nearest rotational quantum state J (where $j = \hbar[J(J+1)]^{1/2}$).

Table VI lists j_{max} for the five real frequency modes of the transition state. The calculated H_2 rotational distribution when $x_{\text{H}_2} = 0$ is shown in Fig. 12(a). When $x_{\text{H}_2} = 0$,

TABLE VI. Transfer of H₂ CO vibrational momentum to product angular momentum for the impulsive model.^a

ν_i	$J_{H_2}^b$	J_{CO}^b	$J_{H_2}^c$	J_{CO}^c
1	5.95	0.54	4.76	0.22
2	0.70	1.77	0.61	1.04
3	0.90	7.01	0.54	7.09
4	3.55	6.61	2.80	6.54
5	2.75	6.27	2.14	6.13

^aUnits of \hbar . The out-of-plane bend is ν_4 .^bTransition state equilibrium geometry.^cEquilibrium geometry 22.4 kcal/mol below transition state.

the impulse does not apply a torque on the H₂, and the parent vibrational motions alone determine the rotational distribution. The calculated distributions for all H₂ vibrational states are the same. The calculated distribution has the general shape of the measured rotational distributions, but the width of the calculated distribution is broader than experiment. Increasing x_{H_2} broadens the calculated J_{H_2} distribution further.

If the exit valley is modeled as an impulsive force, it is most sensible to apply this force at a geometry between that of the transition state and the products, since by definition, the forces at the transition state are zero. A reasonable place to apply the impulse is at a point along the presumed har-

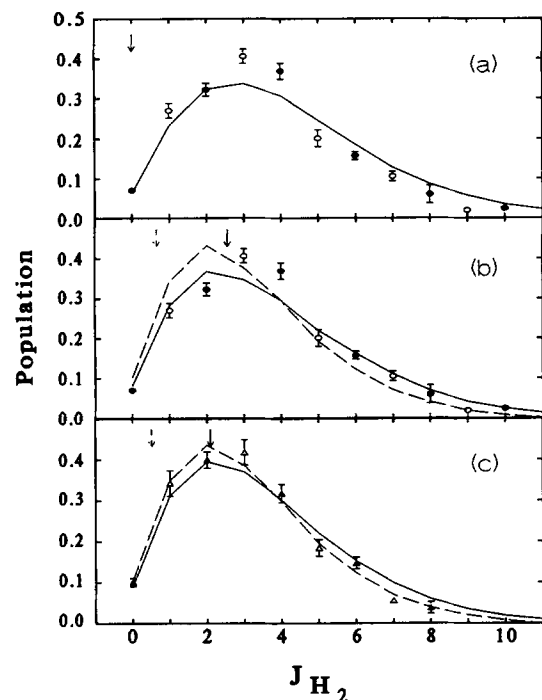


FIG. 12. Impulsive model results for $E_{av1} = 30\,260\text{ cm}^{-1}$. (a) Transition state geometry with $x_{H_2} = 0\text{ Å}$. (b) H₂ ($\nu = 1$) and (c) H₂ ($\nu = 3$) results for the geometry that corresponds to 22.4 kcal/mol below the barrier. The solid lines and arrows are for $x_{CO} = 0.27\text{ Å}$ and $x_{H_2} = 0.09\text{ Å}$; the dashed lines and arrows are for $x_{CO} = 0.27\text{ Å}$ and $x_{H_2} = 0.03\text{ Å}$. The arrows show the J_{H_2} resulting from the impulsive force only. The circles are the measured populations of H₂ ($\nu = 1$) for $2^1 4^1 S_1$ H₂ CO photolysis on the $R_0(0)e$ and $^2P_1(1)\sigma$ lines. The triangles are the corresponding data for H₂ ($\nu = 3$).

monic reaction coordinate where Berry's simple golden rule model^{52,53} best fits the measured H₂ vibrational distribution. In this simple golden rule model, the relative transition probability for formation of final product states is

$$W_{i \rightarrow f} = (2\pi/\hbar) |\langle f|i \rangle|^2 \rho_f(\epsilon), \quad (26)$$

where $\langle f|i \rangle$ is the Franck–Condon overlap integral of the bound “dressed oscillator” wave function and the free rotor wave function, and $\rho_f(\epsilon)$ is the density of final states. The bound dressed oscillator wave function is generated in the following manner. For a given distance along the reaction coordinate, an H–H internuclear distance probability function is generated by randomly selecting phases of the position coordinates for each of the five real frequency modes, which are taken to be the same as at the transition state. Only position coordinates within two times the classical turning points are included: this includes 99% of the probability. The probability of these phases is placed in the 0.01 Å bin corresponding to the H–H distance. This is repeated 1×10^6 times to produce a smooth probability function in 0.01 Å increments. The wave function is the square root of the probability function. The H₂ free rotor is represented by Morse oscillator wave functions.⁵⁴ The density of states function is approximated as being proportional to the square root of the product translational energy.

Calculated vibrational distributions are shown in Fig. 13. The experimental vibrational distribution is best fit with a distance along the reaction coordinate which corresponds to 22.4 kcal/mol below the barrier (29% down from the top of the barrier). The peak of the distribution is a variable which is determined by the distance along the reaction coordinate. The width is determined from the amplitudes of the five other modes, which are derived from the normal mode analysis. Note that at the *ab initio* transition state, the calculated H₂ vibrational distribution peaks at $\nu \approx 3-4$. The CO vibrational distribution is calculated in a similar manner. The calculated $\nu = 0:\nu = 1:\nu = 2$ ratio is 0.86:0.14:0.00 which compares well with the measured distribution of 0.87:0.11:0.02.² Translation along the reaction coordinate has little effect on the CO bond length in the parent, so the calculated CO vibrational distributions for the transition

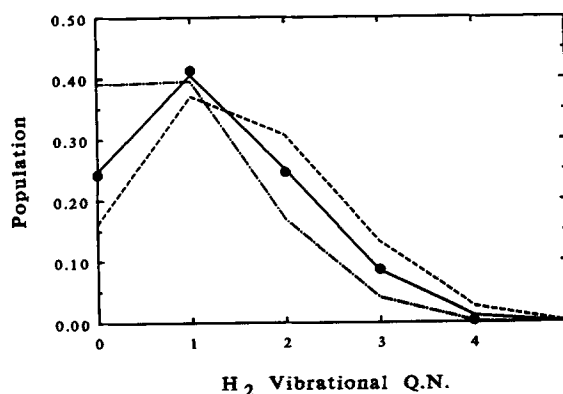


FIG. 13. H₂ vibrational distributions calculated from the golden rule model (Refs. 52 and 53). The solid line corresponds to the geometry 22.4 kcal/mol below the barrier. The dashed and dot-dashed lines correspond to the geometries 16.8 and 30.9 kcal/mol below the barrier, respectively. The points are the measured distribution from Ref. 4.

state geometry and the geometry 22.4 kcal/mol below the transition state are similar.

Figures 12(b) and 12(c) show the calculated J_{H_2} distributions at the geometry 22.4 kcal/mol below the transition state for x_{H_2} values of 0.03 and 0.09 Å. The impulse is applied to give corotating products as is implied by the reaction coordinate (Fig. 10). In both cases a value of $x_{CO} = 0.27$ Å fits the measured J_{CO} distribution. The calculated H_2 ($\nu = 3$) J distribution agrees reasonably well with experiment, but parameters could not be found that simultaneously fit the peak and the width of the H_2 ($\nu = 1$) measured J distribution. The impact parameter calculated from the *ab initio* reaction coordinate varies from 1.01 Å for the equilibrium transition state geometry to 0.94 Å for the geometry 22.4 kcal/mol below the barrier. When $x_{H_2} = 0.03$ Å, the impulsive model impact parameter is 0.85 Å; when $x_{H_2} = 0.09$ Å, $b = 0.91$ Å. The impact parameters used in the model are reasonably consistent with the *ab initio* reaction coordinate.

The contribution of the parent's zero-point vibrational motion to the CO angular momentum is calculated just as for the H_2 . A separate calculation is done for each H_2 vibrational state and the total distribution is weighted by the H_2 golden rule model vibrational distribution. The calculated CO rotational distribution and correlation between H_2 vibration and CO rotation is shown in Fig. 14. The H_2CO geometry corresponds to 22.4 kcal/mol below the barrier; the value $x_{CO} = 0.27 \pm 0.03$ Å fits the peak of the measured CO rotational distribution. The calculated difference of the peak J_{CO} correlated to H_2 ($\nu = 1$) and H_2 ($\nu = 3$) is 6.6 quanta which agrees well with the measured difference of about 6 quanta.

The total energy for 2^1A_1 photolysis is about 1700 cm^{-1} above the barrier to dissociation. This energy is large enough to excite 1 or 2 quanta of the two lowest frequency modes of the transition state ν_4 and ν_5 . Including these excited state motions, with their appropriate weights, would only mod-

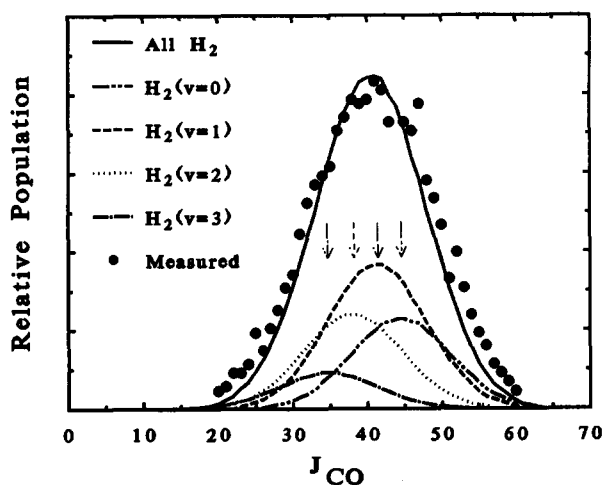


FIG. 14. Calculated CO rotational distribution for $E_{av1} = 30\,260 \text{ cm}^{-1}$. The geometry corresponds to 22.4 kcal/mol below the barrier: $x_{CO} = 0.27$ Å, $x_{H_2} = 0.09$ Å. The arrows show the J_{CO} for the different H_2 vibrational states resulting from the impulsive force only. The measured distribution is from Ref. 3.

estly increase the width of the calculated J_{H_2} distributions. The bulk of the width is from the zero-point motion of the high frequency CH stretch ν_1 .

Product distributions for D_2CO and HDCO photolysis are calculated with no additional parameters. The two transition states of HDCO are weighted equally, though the transition state with the long C-H bond has a zero-point energy 280 cm^{-1} lower than the transition state with the long C-D bond. The geometry corresponding to H_2CO 22.4 kcal/mol below the barrier is used. Both the HD and D_2 calculated vibrational distributions peak in $\nu = 1$. The calculated J_{CO} distributions are compared with the measured distributions in Fig. 15 and the agreement is reasonable.

The J_{D_2} distributions are predicted to be similar to the J_{H_2} distributions, with $J_{\text{peak}} = 3-4$ quanta. Figure 16 shows that the calculated HD rotational distribution is qualitatively different from the J_{H_2} distributions. Because the HD center of mass is shifted from the HD center of symmetry, the impulsive force applies different torques on the HD for the two different transition states. The two transition states produce different distributions and the total distribution is a linear combination of the two. The HD rotational distributions are expected to be sensitive to the forces in the exit valley, unlike the H_2 rotational distributions.

This impulsive model has three parameters: x_{H_2} , x_{CO} , and the point along the reaction coordinate where the impulse is applied. These three parameters directly determine the calculated peaks of the J_{H_2} , J_{CO} , and H_2 vibrational distributions, but the widths of all three distributions are determined from the *ab initio* parent vibrational motions. With no extra parameters, the impulsive model matches the observed

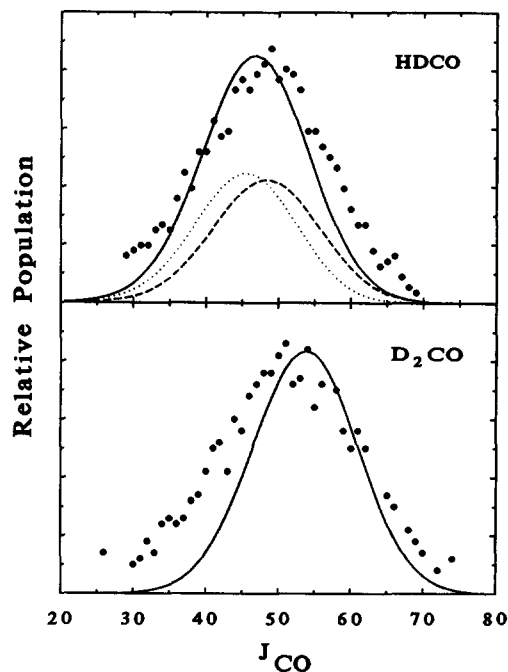


FIG. 15. Calculated CO rotational distributions from photolysis of HDCO and D_2CO . The parameters used are $E_{av1} = 30\,260 \text{ cm}^{-1}$, $x_{H_2} = 0.090$ Å, $x_{CO} = 0.27$ Å. In the HDCO calculation, the short-dashed line is the distribution from the transition state with the long C-H bond and the long-dashed line is from the transition state with the long C-D bond. The points are the measured distributions from Ref. 3.

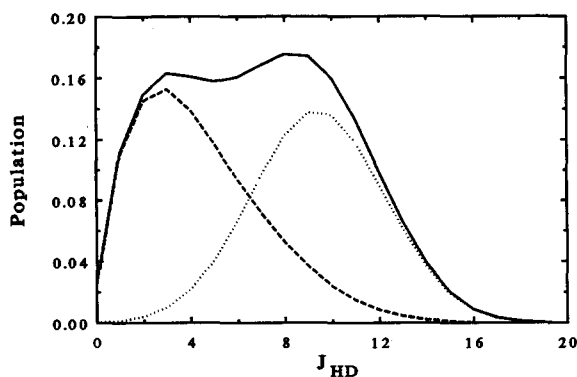


FIG. 16. Calculated HD rotational distribution from photolysis of HDCO using the same parameters as Fig. 15. The short-dashed line is the distribution from the transition state with the long C-H bond and the long-dashed line is from the transition state with the long C-D bond.

correlation between the H_2 vibrational state and J_{CO} as well as the change of the J_{CO} distribution upon isotopic substitution. A simple approach like this will not reproduce the effects of subtle details in the shape of the reaction surface or in the quantum dynamics of passing through the transition state. The possible difference in the J_{CO} distributions from photolysis on the ${}^1R_0(0)e$ and ${}^2P_1(1)o$ lines of $2^14^1S_1$ H_2 CO requires a considerably more complete dynamical theory. However, this simple model is physically reasonable and reproduces the general features of the measured product state distributions.

C. Schinke's semiclassical theory

Schinke has reproduced the J_{CO} distributions from photolysis of H_2 CO, HDCO, and D_2 CO using an *ab initio* H_2 -CO scattering potential and an elegant theory based on the infinite order sudden approximation.¹² The corresponding calculated rotational distribution for *ortho* H_2 peaks 1-2 quanta higher than measured here and the data does not support the bimodal distribution predicted for *para* H_2 .¹¹ Schinke's calculation is based on determining the probability and hence the distribution of product states from the infinite order sudden photodissociation amplitude. The initial expression for the dissociation cross section is the golden rule:

$$\sigma^{if} \propto \langle \Psi_{gr}^i | \mu | \Psi_{ex}^f \rangle, \quad (27)$$

where Ψ_{gr}^i is the initial parent state, Ψ_{ex}^f is the excited parent state which correlates with the final product state f , and μ is the transition moment.¹³ Because H_2 CO predissociates, Schinke replaces the ground state wave function with that of the H_2 CO transition state. The final expression for the H_2 photodissociation amplitude is¹¹

$$t(j) = \int d\gamma \sin \gamma Y_{j0}(\gamma, 0) \phi(\gamma) \exp[i\eta(\gamma)]. \quad (28)$$

Here, γ is the angle between the H_2 axis and the line connecting the H_2 and CO center of masses. The product state distribution, $P(j) = |t(j)|^2$, depends on the angular dependence of the transition state $\phi(\gamma)$, the spherical harmonic, $Y_{j0}(\gamma, 0)$, and the radial integral, $\exp[i\eta(\gamma)]$, where $\eta(\gamma)$ is

well approximated by the phase shift of ordinary scattering. The radial integral integrates the transition state and excited state radial wave functions over the potential surface, expressing the final state interactions in the exit valley. Schinke uses an *ab initio* $H_2(v=0)$ -CO($v=0$) scattering surface for this potential. However, since H_2 is quite spherical, this integral has little angular dependence and can be neglected in the rotational distribution calculation. Therefore, Eq. (28) can be further simplified to give

$$t(j) = \int d\gamma \sin \gamma Y_{j0}(\gamma, 0) \phi(\gamma) \quad (29)$$

which is a Franck-Condon overlap integral applied to in-plane rotation. Schinke made the approximation in these calculations that the dissociation occurs in the plane of the molecule. This restricts the above equations to the case when $m=0$, as indicated by $Y_{jm}(\gamma, \chi) = Y_{j0}(\gamma, 0)$. The *ab initio* transition state geometry and in-plane zero-point normal modes are used to calculate $\phi(\gamma)$ in one degree increments. The resulting J_{H_2} distribution is shown in Fig. 17(a) and is very similar to Schinke's result.

Nonplanar contributions are included by replacing the wave function $\phi(\gamma)$ with $\phi(\gamma, \chi)$, where the torsional angle χ is the angle between the two planes which contain the H-H internuclear axis and the C-O internuclear axis and share the line connecting the H_2 and CO centers of mass. The scattering amplitude is then

$$t(j, m) = \int_0^{2\pi} \int_0^\pi Y_{jm}(\gamma, \chi) \phi(\gamma, \chi) \sin(\gamma) d\gamma d\chi. \quad (30)$$

$P(j)$ is calculated by summing $|t(j, m)|^2$ over all m levels.

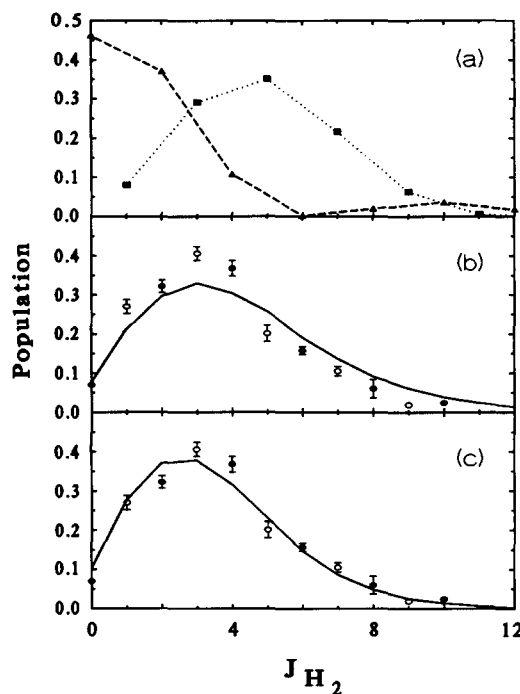


FIG. 17. Schinke model results. (a) Transition state geometry with in-plane motions only; (b) Transition state geometry with out-of-plane motions included; (c) Geometry corresponding to 22.4 kcal/mol below the barrier. The circles are the measured populations for $2^14^1S_1$ H_2 CO photolysis on the ${}^1R_0(0)e$ and ${}^2P_1(1)o$ lines.

The *ab initio* transition state geometry and zero-point vibrational modes are used to numerically calculate $\phi(\gamma, \chi)$ in one degree increments of γ and χ . The resulting H_2 rotational distribution is shown in Fig. 17(b). Including the out-of-plane motions of the transition state gives distributions that are singly peaked with *ortho* and *para* H_2 lying on the same curve, in agreement with experiment. The restriction to motion in a plane caused the bimodal character of Schinke's prediction for the *para* H_2 rotational distribution. The calculation shown in Fig. 17(b) is the quantum analog of the classical calculation shown in Fig. 12(a). They are both Franck-Condon overlaps applied to rotations. Both methods give essentially the same results, even at low J . Figure 17(c) shows the calculation for the geometry 22.4 kcal/mol below the transition state. Both the classical impulsive model and Schinke's model calculations result in cooler rotational distributions when the H-H distance is shortened in the parent equilibrium geometry.

Schinke's model reproduces the shapes and magnitudes of both the H_2 and CO rotational distributions with no adjustable parameters, which is a remarkable result. Like the impulsive model, Schinke's model predicts D_2 rotational distributions that are similar to the J_{H_2} distributions and a bimodal HD rotational distribution.¹¹ To calculate the product correlation between H_2 vibration and CO rotation, a potential for H_2 ($v = 1, 2, 3$) scattering with $CO(v = 0)$ is needed, but is not presently available. Schinke's model predicts very little correlation between J_{CO} and J_{H_2} .¹¹ The uncertainties in the data are too large to confirm or contradict this prediction of the model.

It seems reasonable that normal mode motions of the transition state would lead to considerable out-of-plane character in the dissociation. This is born out by recent vector correlation measurements.²⁷ If the dissociation occurred purely in the plane, the H_2 velocity vector v and its rotational vector J would be perpendicular to each other. However, the v - J correlation is not at the limit of $v \perp J$, but rather intermediate between $v \parallel J$ and $v \perp J$.

VI. CONCLUSIONS

Doppler-resolved LIF spectroscopy allows the simultaneous measurement of H_2 alignment, rotational populations, and H_2 (v, J) average velocities. The fragment alignment is not completely washed out by rotation during the long lifetime of the excited state parent molecule. The rotational distributions of *ortho* and *para* H_2 from photolysis of H_2CO near the barrier to dissociation are Boltzmann-like and nearly identical. The $H_2CO(S_1)$ vibrational state has little influence on the J_{H_2} distributions, but there is evidence that photolysis of higher rotational states of $H_2CO(S_1)$ results in warmer J_{H_2} distributions. There is little influence of the nuclear spin state on the shapes of the J_{H_2} distributions. *Para* and *ortho* H_2 are not interconverted but otherwise behave similarly in the dissociation and respond to the same potential forces. The coupling of the S_1 and S_0 surfaces must be insensitive to nuclear spin. For photolysis of $2^1A'$ S_1 H_2CO , a product quantum state correlation is deduced from the average velocity measurements: higher vibrational states of H_2 are correlated with lower rotational states of CO.

The $H_2(v, J)$ and $CO(v, J)$ distributions as well as the correlation between H_2 vibrational states and CO rotational states is modeled reasonably well by an impulsive dissociation near the transition state. The semiclassical model has three parameters: the effective H_2 and CO impact parameters, and the position of the impulsive force along the reaction coordinate. The anisotropy of the potential felt by the CO is clearly much larger than that felt by the H_2 . The coupling of parent zero-point vibrational motions at the transition state to the product angular momentum accounts for the observed product distribution widths.

The *para* H_2 rotational distribution is not bimodal as had been predicted by Schinke. The bimodal prediction was a result of restricting the dissociation to a plane. Schinke's model matches the measured H_2 rotational distribution if parent out-of-plane motions are included in the calculation. Both Schinke's model and the semiclassical impulsive model predict bimodal HD rotational distributions from photolysis of HDCO.

In the future, we will present data on the vector correlations of the photodissociation process, including spatial anisotropy and velocity-rotation correlations. These studies offer further insights into the dissociation picture.

ACKNOWLEDGMENTS

We thank several colleagues for theoretical help, including Dr. Lin Chen and Dr. Robert Snyder for use of their normal mode program, Dr. Nancy Makri for helpful discussions and especially Professor William H. Miller for his guidance concerning the trajectory studies. This research was supported by U.S. National Science Foundation Grant No. CHE88-16552. T.J.B. acknowledges support from the U.S. National Science Foundation in the form of a predoctoral fellowship. K.L.C. and C.B.M. thank the Adolph C. and Mary Sprague Miller Foundation for a postdoctoral fellowship and a research professorship, respectively.

- ¹C. B. Moore and J. C. Weishaar, *Ann. Rev. Phys. Chem.* **34**, 525 (1983).
- ²P. L. Houston and C. B. Moore, *J. Chem. Phys.* **65**, 757 (1976).
- ³D. J. Bamford, S. V. Filseth, M. F. Foltz, J. W. Hepburn, and C. B. Moore, *J. Chem. Phys.* **82**, 3032 (1985).
- ⁴D. Debarre, M. Lefebvre, M. Pealat, J.-P. E. Taran, D. J. Bamford, and C. B. Moore, *J. Chem. Phys.* **83**, 4476 (1985).
- ⁵M. Pealat, D. Debarre, J.-M. Marie, J.-P. E. Taran, A. Tramer, and C. B. Moore, *Chem. Phys. Lett.* **98**, 299 (1983).
- ⁶J. D. Goddard and H. F. Schaefer III, *J. Chem. Phys.* **70**, 5117 (1979).
- ⁷J. D. Goddard, Y. Yamaguchi, and H. F. Schaefer III, *J. Chem. Phys.* **75**, 3459 (1981).
- ⁸M. Dupuis, W. A. Lester, B. H. Lengsfeld, and B. Liu, *J. Chem. Phys.* **79**, 6167 (1983).
- ⁹M. J. Frisch, R. Krishnan, and J. A. Pople, *J. Phys. Chem.* **85**, 1467 (1981).
- ¹⁰P. Ho, D. J. Bamford, R. J. Buss, Y. T. Lee, and C. B. Moore, *J. Chem. Phys.* **76**, 3630 (1982).
- ¹¹R. Schinke, *J. Chem. Phys.* **84**, 1487 (1986).
- ¹²R. Schinke, *Chem. Phys. Lett.* **120**, 129 (1985).
- ¹³R. Schinke, V. Engel, and V. Staemmler, *J. Chem. Phys.* **83**, 4522 (1985); R. Schinke and V. Engel, *ibid.* **83**, 5068 (1985); R. Schinke, *Ann. Rev. Phys. Chem.* **39**, 39 (1988); R. Schinke, H. Meyer, U. Buck, and G. H. F. Dierksen, *J. Chem. Phys.* **80**, 5518 (1984).
- ¹⁴K.-H. Gericke, *Phys. Rev. Lett.* **60**, 561 (1988).

- ¹⁵W. Zapke, D. Cotter, and U. Brackmann, *Opt. Commun.* **36**, 79 (1981).
- ¹⁶R. Spence and W. Wild, *J. Chem. Soc. (London)* **1935** 338.
- ¹⁷The notation $2_0^2 4_0^3$ refers to absorption from the vibronic origin of S_0 ($v_1'' = \dots = v_6'' = 0$) to the vibrational level having 1 quantum of v_2 ($v_2' = 1$) and 3 quanta of v_4 ($v_4' = 3$) in S_1 . Since all transitions in this work originate in the ground vibronic level, the subscript 0 is omitted.
- ¹⁸B. Schramm, D. J. Bamford, and C. B. Moore, *Chem. Phys. Lett.* **98**, 305 (1983).
- ¹⁹The notation ${}^o Q_{K_o}(J'')$ denotes a $\Delta K_o = +1$, $\Delta J = 0$ transition in absorption from the $J'' K''_o$ ground state. Symbols o and e indicate whether $J'' + K''_o + K''_e$ is odd or even. The rotational states are denoted J_{K_o, K_e} , where K_o and K_e are the K quantum numbers of the state in the prolate and oblate symmetric top limits.
- ²⁰D. J. Clouthier and D. A. Ramsay, *Ann. Rev. Phys. Chem.* **34**, 31 (1983).
- ²¹I. Dabrowski, *Can. J. Phys.* **62**, 1639 (1984).
- ²²F. J. Northrup, J. C. Polanyi, S. C. Wallace, and J. M. Williamson, *Chem. Phys. Lett.* **105**, 34 (1984).
- ²³R. Hilbig and R. Wallenstein, *Appl. Opt.* **21**, 913 (1982).
- ²⁴C. R. Vidal, in *Tunable Lasers*, edited by L. F. Mollenauer and J. C. White, *Topics in Applied Physics* **59** (Springer, New York, 1987).
- ²⁵R. N. Dixon, *J. Chem. Phys.* **85**, 1866 (1986).
- ²⁶K.-H. Gericke, S. Klee, F. J. Comes, and R. N. Dixon, *J. Chem. Phys.* **85**, 4463 (1986).
- ²⁷T. J. Butenhoff, K. L. Carleton, M.-C. Chuang, and C. B. Moore, *J. Chem. Soc. Faraday Trans. 2* **85**, 1155 (1989).
- ²⁸K. L. Carleton, T. J. Butenhoff, and C. B. Moore (unpublished).
- ²⁹C. H. Greene and R. N. Zare, *J. Chem. Phys.* **78**, 6741 (1983).
- ³⁰C. H. Greene and R. N. Zare, *Ann. Rev. Phys. Chem.* **33**, 119 (1982).
- ³¹D. Villarejo, R. Stockbauer, and M. G. Inghram, *J. Chem. Phys.* **50**, 1754 (1969).
- ³²R. E. Drullinger and R. N. Zare, *J. Chem. Phys.* **51**, 5532 (1969).
- ³³W. E. Henke, H. L. Selzle, T. R. Hays, E. W. Schlag, and S. H. Lin, *J. Chem. Phys.* **76**, 1327 (1982).
- ³⁴M. Suto, X. Wang, and L. C. Lee, *J. Chem. Phys.* **85**, 4228 (1986).
- ³⁵D. L. Baulch, R. A. Cox, P. J. Crutzen, R. F. Hampson, J. A. Kerr, J. Troe, and R. T. Watson, *J. Phys. Chem. Ref. Data* **11**, 327 (1982).
- ³⁶R. A. Fletcher and G. Pilcher, *Trans. Faraday Soc.* **66**, 794 (1970).
- ³⁷The discrepancy between the product correlations given here and those in Ref. 27 arises from incorrectly using $\Delta H(0\text{ K}) = -0.47$ kcal/mol in Ref. 27.
- ³⁸H. G. Kolsky, T. E. Phipps, Jr., N. F. Ramsey, and H. B. Silsbee, *Phys. Rev.* **87**, 395 (1952).
- ³⁹T. Nagata, T. Kondow, K. Kuchitsu, G. W. Loge, and R. N. Zare, *Mol. Phys.* **50**, 49 (1983).
- ⁴⁰W. F. Polik, D. R. Guyer, and C. B. Moore, *J. Chem. Phys.* (in press); W. F. Polik, D. R. Guyer, W. H. Miller, and C. B. Moore, *J. Chem. Phys.* (in press).
- ⁴¹The different H_2 line shapes for the $P(1)$ and $R(1)$ lines are caused by the v - J correlation. See Ref. 28.
- ⁴²R. D. Levine and R. B. Bernstein, *Molecular Reaction Dynamics and Chemical Reactivity* (Oxford University, New York, 1987).
- ⁴³D. J. Bamford, Ph.D. thesis, University of California, Berkeley, 1984.
- ⁴⁴P. Pechukas and J. C. Light, *J. Chem. Phys.* **42**, 3281 (1965).
- ⁴⁵I.-C. Chen, W. H. Green and C. B. Moore, *J. Chem. Phys.* **89**, 314 (1988).
- ⁴⁶N. C. Handy and S. Carter, *Chem. Phys. Lett.* **79**, 118; **83**, 216 (1981).
- ⁴⁷The frequencies and reaction coordinate v_6 do not agree well with those from Goddard and Schaefer (Ref. 6) but do agree well with the DZ SCF frequencies and reaction coordinate listed in Goddard, Yamaguchi, and Schaefer (Ref. 7).
- ⁴⁸D. R. Guyer, W. F. Polik, and C. B. Moore, *J. Chem. Phys.* **84**, 6519 (1986).
- ⁴⁹W. H. Miller (private communication).
- ⁵⁰G. E. Busch and K. R. Wilson, *J. Chem. Phys.* **56**, 3626 (1972).
- ⁵¹H. B. Levene and J. J. Valentini, *J. Chem. Phys.* **87**, 2594 (1987).
- ⁵²M. J. Berry, *Chem. Phys. Lett.* **29**, 329 (1974).
- ⁵³M. J. Berry, *J. Chem. Phys.* **61**, 3114 (1974).
- ⁵⁴P. M. Morse, *Phys. Rev.* **34**, 57 (1929).